AN INVERSION-LAYER MOBILITY MODEL FOR CODECS

by

David A. Gates

Memorandum No. UCB/ERL M90/96

26 October 1990

AN INVERSION-LAYER MOBILITY MODEL
FOR CODECS

by

David A. Gates

Memorandum No. UCB/ERL M90/96

26 October 1990

ELECTRONICS RESEARCH LABORATORY

College of Engineering
University of California, Berkeley
94720

Contents

Abstract

Inversion-layer mobility in MOS transistor channels has been investigated in order to improve its modelling in the CODECS mixed-level circuit and device simulator. Several scattering mechanisms that affect this mobility are reviewed. The inversion-layer mobility can be modelled by its dependencies on the normal and lateral components of the electric field in the channel. Based on this approach, an inversion-layer-specific mobility model has been added to CODECS. A new empirical relation is used to describe the normal-field dependence of the mobility. The new expression has been tested by comparison to experimental data. The accuracy of simulation of MOSFET I_{DS} - V_{GS} characteristics in the linear region is improved by the new model.

Acknowledgements

I thank my research advisor, Professor Donald Pederson, for his support and guidance during my years at Berkeley. He allowed me the freedom to choose my own way and take my own time, but was always there when I needed his encouragement most. In addition, whenever my ambitions outran my reason, he was able to bring me back to my senses.

Professor Ping Ko has shown continued interest in the progress of this research. My discussions with him about this project were very beneficial, and I thank him for his timely advice and for reading this report.

I would also like to express my gratitude to Professor Robert Dutton and his colleagues at Stanford University. My visit with them provided a critical boost of energy that set me going at a time when my spirits were especially low.

Many Berkeley graduate students have helped me while I pursued this research. I thank most of all Dr. Kartikeya Mayaram, now with Texas Instruments, for teaching me the ins and outs of the CODECS program. Without his technical expertise, this project would never have come to fruition. In addition, Dr. Theologos Kelessoglou has been very patient in answering all my IATEX questions. I owe the "look and feel" of this report to him. Other members of my research group: Hoa

Chapter 1

Introduction

Accurate simulation of MOS devices requires a good model for the inversion-layer mobility. Degradation of the inversion-layer mobility in the presence of high normal electric fields has been demonstrated by many authors [SABN79, SUN80, LIAN86, WATT87, LEE89]. Shrinking gate oxide thicknesses and increasing substrate doping concentrations increase the average normal field and consequently the magnitude of this degradation. The original version of the CODECS mixed-level circuit and device simulator [MAYA88] does not contain a mobility model which includes this effect. In fact, the original mobility model does not treat the MOSFET inversion layer as a special case. The original model is best suited to simulation of the mobility in the silicon bulk. A new inversion-layer-specific mobility model has been formulated and integrated with the original mobility model. The new model explicitly models normal-field mobility degradation. This report describes the physical basis of the new model and its design and implementation in the CODECS device simulator, DSIM. Experiments which test the accuracy of its normal-field dependence are also presented.

In Chapter 2, the fundamental physical basis of the mobility is explored. The mobility is related to a scattering process which limits the drift velocity of mobile carriers. Matthiesen's rule for combining the effects of more than one scattering mechanism on the mobility is introduced. Several scattering processes which are important in inversion layers are reviewed. Particular attention is paid to surface

roughness scattering because it is not modelled by the original CODECS mobility expressions.

In Chapter 3, the inversion-layer mobility is reconsidered in terms of modelling its behavior. Variation of the mobility with respect to changes in the electric field within an inversion layer is emphasized. An approach to modelling the mobility by decomposing the electric field into orthogonal components is described. The scattering mechanisms are categorized according to their dependence or independence from changes in the field components. Methods for modelling the field dependence of the mobility are reviewed. Again, emphasis is placed on material not addressed by the original CODECS mobility model.

In Chapter 4, two new inversion-layer mobility models for the CODECS device simulator, DSIM, are presented. Each model is based on a different approach to modelling the normal-field dependence. Attention is paid to the constraints imposed by this specific device simulator on the form and implementation of the mobility models. The impact of the new models on the structure of the numerical algorithms in the simulator is outlined. The results of experiments that tested the viability of various design alternatives are given.

In Chapter 5, the validity of the normal-field dependencies of the new models are tested by comparison to experimental data. Testing is restricted to the linear region of MOSFET operation, where normal-field mobility degradation is most important. A procedure for extracting the effective inversion-layer mobility from simulation results is given. This procedure is contrasted with the experimental methods used by Watt and Plummer [WATT87] to determine the effective mobility. Simulations intended to reproduce their experimental results were performed. When the experimentally determined and simulated effective mobilities are plotted together, reasonable agreement is observed for both models. However, one of the approaches is substantially more accurate than the other approach. The accuracies of both new models are compared to that of the original CODECS mobility model. Comment is made on discrepancies between the simulated mobility and the experimentally determined mobility when the less accurate approach is used.

In Appendix A, the new expressions for the inversion-layer mobility and its

derivatives with respect to the components of the electric field are given. Appendix B is a supplement to the original CODECS user's manual which describes the user-interface changes due to the new mobility model. Appendix C overviews the DSIM device simulator, with emphasis on information relevant to the new inversion-layer mobility model.

Chapter 2

Overview of Inversion-Layer Mobility Theory

2.1 Summary

The mobility of an electron is an important physical property related to its ability to move about freely within a material. A higher mobility indicates that an electron is moved faster by a given driving force. The inversion-layer mobility is a special case of this property where the mobile electrons are confined to a MOSFET inversion layer. In this chapter, attention is restricted to electron inversion layers. However, analogous arguments exist for hole inversion layers.

First, an idealized situation is considered where the mobility is related to other basic properties of the electron and its environment. The role of momentum scattering in limiting the mobility is emphasized. When more than one scattering mechanism is responsible for limiting the mobility, some method is needed to combine the effects of the different mechanisms. If the mechanisms are independent, the mobility can be determined using Matthiessen's rule.

Several scattering mechanisms affect the inversion-layer mobility when the driving force is not large. The connections between each of these mechanisms and the motion of electrons are examined. The relative importance of each mechanism in determining the overall mobility is also established. An experimentally determined

inversion-layer mobility curve is described in terms of these mechanisms. Finally, velocity saturation in an inversion layer is considered as a consequence of the existence of large carrier driving forces.

2.2   Definition of Mobility

Consider a uniform sample of silicon at thermal equilibrium. Electrons in the silicon move about randomly due to thermal excitation. The so-called thermal velocity, v_{th}, of these electrons can be roughly calculated by equating the classical kinetic energy of a moving body, $\frac{1}{2}mv^2$, to the average thermal energy of a particle in an ideal gas, $\frac{3}{2}kT$ [MULL86]. Numerically, v_{th} is approximately $10^7 cm/s$ at room temperature, $300°K$. The thermal velocity is an averaged property of the moving electrons; the actual motion is interrupted by countless collisions between the moving electron, other electrons, and the silicon lattice itself. This collision process is known as *scattering*. At thermal equilibrium, no single direction is preferred by this process, and the mean position of an electron is constant.

The average time between collisions is an important factor in determining mobility and is represented by the symbol τ. During the intercollision period, τ, the electron moves at the thermal velocity, v_{th}, and covers a distance $l = v_{th}\tau$, the mean free path of an electron. Both l and τ are used when describing and quantifying the scattering behavior of electrons.

2.2.1   Drift Velocity

When a suitably small electric field is applied uniformly within the silicon, the motion of the electrons is slightly perturbed due to the force of the applied field. The particles are no longer stationary on average, but instead move in the direction of the applied field. The net velocity of the electrons in this direction is known as the *drift velocity*, v_d. The drift velocity is determined by multiplying the acceleration on an electron due to an electric field E: $a = -qE/m^*$, by the time of free acceleration,

τ, to arrive at:

$$v_d = \frac{-qE\tau}{m^*} \tag{2.1}$$

where q is the electron charge, and m^* is the electron drift mass in the silicon lattice. The mobility, μ, is defined as the ratio of the drift velocity to the magnitude of the applied field, and is given by:

$$\mu = \frac{q\tau}{m^*} \tag{2.2}$$

It is apparent that the value of τ directly affects the value of the mobility, and thus characterization of scattering mechanisms can supply information about the mobility. This argument relies on two assumptions which should be explicitly recognized:

- The applied field must be small, so that the average velocity, mean scattering time, and mean free path remain largely unaffected.

- The silicon sample and the strength and direction of the field within the silicon are uniform.

Unfortunately, the conditions in an inversion layer do not satisfy these assumptions. As a result, the basic mobility definition is not directly applicable. However, the concept of scattering is still useful when examining the inversion-layer mobility.

2.3 Matthiesen's Rule

In an actual sample of silicon, multiple mechanisms can act to scatter the motion of electrons. The mobility due to these various mechanisms is often a complex function of their respective mean scattering times. Considered separately, a mean scattering time, τ_i, can be defined for each mechanism, and individual mobilities, μ_i, can be calculated using the original mobility definition, Equation 2.2. At this point, the additional assumption that the scattering processes are independent can be made. Then, the overall scattering time is given by [NISH87]:

$$1/\tau = 1/\tau_1 + \cdots + 1/\tau_n \tag{2.3}$$

where n independent scattering processes are involved. The overall mobility is given by:

$$1/\mu = m^*/q\tau = 1/\mu_1 + \cdots + 1/\mu_n \qquad (2.4)$$

This is the Matthiesen Rule for combining the effects of multiple scattering processes. In physical situations, the mechanisms are not always independent, and a heuristic variation, the Matthiesen Rule of order M, is occasionally used in mobility models:

$$1/\mu^M = 1/\mu_i{}^M + \cdots + 1/\mu_n{}^M \qquad (2.5)$$

This expression is only an approximation to the true relationship determining the mobility, and more accurate but difficult to use expressions are sometimes available [SELB85].

2.4   Surface Scattering Mechanisms

Figure 2.1 shows an idealized representation of an inversion layer where three inversion-layer scattering mechanisms are identified: lattice vibration scattering, ionized impurity scattering and surface roughness scattering. These three processes dominate for low applied fields in the direction of current flow [SUN80]. Of the three, surface roughness scattering is believed responsible for normal-field mobility degradation. When higher fields are applied, a fourth mechanism, hot carrier scattering, begins to operate. This mechanism affects only high-energy electrons and causes saturation of the drift velocity. Physical descriptions of each these mechanisms are provided in the following sections.

2.4.1   Lattice Vibration Scattering

A perfectly motionless silicon lattice would never scatter the motion of electrons. However, at any temperature above absolute zero, the lattice vibrates in distinct modes called *phonons*, each of which carries a discrete amount of energy. Electrons travelling through a vibrating lattice interact with these phonons and transfer some of their additional drift-supplied energy. Lattice vibrations are greater at higher

temperatures. As a result, the mobility decreases as a function of temperature due to reduction of the mean scattering time. At room temperature, this mechanism plays an important role in determining the overall mobility.

2.4.2   Ionized Impurity Scattering

When an MOS inversion layer is formed, it is created on the silicon side of the Si-SiO2 interface. The silicon substrate is doped with impurity atoms which ionize at room temperature. These ionized impurities carry charge and are capable of exerting force on mobile electrons. This force and the random distribution of impurity atoms contribute to electron scattering. However, experimental evidence [WATT87] indicates that the inversion-layer mobility is not noticeably affected by the presence of these impurities, except at the highest levels of substrate doping. It is thought that this is due either to the normally low number of impurities actually present within an inversion layer, or to screening of the charge on these impurities by relatively high inversion-layer electron densities. In contrast, ionized impurity scattering has long been recognized as a significant contributor to the mobility far from the surface in the silicon bulk [SELB85].

2.4.3   Surface Roughness Scattering

The conventional picture of the Si-SiO2 interface is one of abrupt change from silicon to oxide, as depicted in Figure 2.2a. This picture embodies the idea of a smooth planar junction between the two materials. However, an actual interface does not conform to this ideal. Instead the surface is generally somewhat rough, as shown in Figure 2.2b. As a result, the silicon lattice structure is deformed near the interface so that bonds are often missing or weakened. While variation of the interface is limited compared to the overall dimensions of an MOS device, electrons in an inversion layer react to this irregularity. Mobile electrons lose momentum by colliding with imperfections in the interface. A more irregular surface leads to stronger surface roughness scattering.

Irregularity in the interface is only one factor which determines the influence

of this scattering mechanism on the overall mobility. Also important is the amount of time an electron spends in the vicinity of the interface. An inversion layer is formed when a strong electric field normal to the interface draws electrons toward the surface. The supply of holes normally found in the p-type substrate has been eliminated, forming the surface *depletion layer*. The force of the normal electric field is balanced by the tendency of electrons to diffuse away from regions of high concentration near the interface to regions of low concentration deeper in the silicon. Thus, an intrinsic element in an inversion layer is a component of the electric field which does not contribute to the drift velocity of the electrons. Instead, it is responsible for the presence of mobile electrons at the surface. This normal field is almost perpendicular to the direction of current flow in a MOSFET channel.

The normal electric field can be used to measure indirectly the width of the inversion layer. The stronger the normal field is, the closer the electrons are to the interface. Because mobile electrons cannot escape from the inversion layer, the mean free path of the electrons is often estimated to be a small multiple of the width of the inversion layer.

2.4.4 Overall Low-Applied-Field Mobility

Experiments by various authors [SUN80, LIAN86, WATT87] indicate that the inversion-layer mobility is degraded in the presence of strong normal fields. Surface roughness scattering is one field-dependent mechanism which may be responsible for this mobility degradation. Figure 2.3 shows the electron inversion-layer mobility data of Watt and Plummer [WATT87]. The mobility was determined in the presence of low driving electric fields. The data is plotted as a function of an effective normal field. The effective normal field is the average of the field at the surface and the field at the lower, or bulk, edge of the inversion layer:

$$E_\perp^{eff} = \left(\frac{E_\perp^{surf} + E_\perp^{bulk}}{2} \right) \tag{2.6}$$

Due to the presence of uncompensated charge in the inversion layer, the normal field strength decreases as distance from the interface increases. Thus, $E_\perp^{surf}$ and $E_\perp^{bulk}$

often have widely different values.

Figure 2.3 clearly shows reduction of the inversion-layer mobility as the effective normal field is increased. In addition, the effect of varying substrate dopant concentration is largely expressed as a change in the initial value of the effective field. However, at the highest substrate doping concentration, the mobility is slightly degraded near the field's initial value. The authors attribute this to scattering of low-density mobile electrons by high-density ionized impurities. When for simplicity this discrepancy is ignored, it can be said that the mobility is a unique function of the effective normal field. The mobility increases as the effective field decreases because of diminished surface roughness scattering. Eventually, while not shown on the figure, the mobility is limited by lattice vibration scattering. However, the exact value of this limited mobility at zero effective field is impossible to determine from Figure 2.3.

2.4.5   Hot Carrier Scattering

The component of the electric field in the same direction as the flow of current is called the lateral electric field. In the derivation of the mobility in Section 2.2, it is assumed that the lateral electric field is small and that the drift velocity attained is only a small fraction of the thermal velocity. As the applied lateral field increases, inversion-layer electrons begin to attain significant drift velocities. In such cases, the electron energy rises well above its ambient thermal energy. These high-energy electrons are called *hot carriers*. The increased energy of these carriers excites new high-energy lattice vibrations. These optical phonons transfer energy away from the electrons very effectively and restrict the attainable electron energy. This scattering process is also largely responsible for velocity saturation, a limitation of the drift velocity, v_d, in the presence of high fields. The reduced scattering time of hot carriers also limits the mobility. The scattering time is reduced because fast hot-carriers can travel the mean scattering length more quickly than carriers at thermal equilibrium.

Figure 2.4 shows a simplified plot of the drift velocity as a function of applied lateral field. At very low fields, the velocity is proportional to the field strength, and the slope of the curve is the low-field mobility. At higher values, the velocity

reaches a limit and the mobility becomes inversely proportional to the field. Velocity saturation occurs in both bulk material and surface inversion layers. Although the experimental evidence is not completely clear, it is generally assumed that the saturation velocity in both cases is approximately the same. Doubt in this hypothesis is caused by difficulties in measuring the inversion-layer drift velocity for high applied fields [YAMA83].

Chapter 3

Inversion-Layer Mobility Modelling

3.1 Summary

In the previous chapter, several inversion-layer scattering mechanisms are reviewed. Unfortunately, in a device simulator it is necessary to define the overall mobility, not just the mechanisms that influence it. In this chapter, another approach to decomposing the mobility is introduced. This new approach is based on separation of the electric field into two fundamental components. The first component, the normal field, draws carriers towards the interface and creates an inversion-layer. The second component, the lateral field, is perpendicular to the first, and drives carriers from one end of the channel to the other. In this context, the inversion-layer mobility is often referred to as field-dependent.

For purposes of modelling, the inversion-layer scattering mechanisms are each recategorized into one of three groups:

- Mechanisms independent of both field components.

- Mechanisms dependent on the normal field.

- Mechanisms dependent on the lateral field.

Each group is then considered separately, in terms of effects on the overall mobility and definition of relevant fields when necessary. Particular attention is paid to the normal-field dependence, since the original CODECS mobility model does not model this behavior.

This approach allows the mobility to be expressed not as an ill-defined function of scattering mechanisms, but rather as a function of measurable components of the field. A particular implementation of an inversion-layer mobility model using this approach is described in the following chapter. In that implementation, the mobility model also uses a synthesizing relation which combines the individual contributions from each field dependence.

3.2 Field-Independent Mobility

Both lattice vibration scattering and ionized impurity scattering are essentially independent of the normal and lateral fields. Lattice vibration scattering is instead primarily dependent on temperature, while ionized impurity scattering is primarily dependent on dopant concentrations. However, it is difficult, if not impossible, to isolate scattering caused by these mechanisms from scattering due to surface roughness. All three mechanisms act in concert. In light of this, it is easiest to model the field-independent mobility with a constant, μ_0. This constant models the lattice-vibration-scattered mobility, which, for a given temperature, is fixed. While ionized impurity scattering becomes noticeable at high dopant concentrations, this model ignores that dependence, resulting in only a slight loss of accuracy. The value of μ_0 is determined at the same time as the normal-field-dependent mobility model parameters.

3.3 Normal-Field-Dependent Mobility

The field which creates the channel and forces the carriers to remain in the vicinity of the rough and irregular surface is variously known as the normal, transverse, or perpendicular electric field. All of these names derive from the fact that

this field is perpendicular to the direction of flow of the carriers as they move from source to drain in a MOSFET. Surface roughness scattering is indirectly related to the magnitude of the normal field through the field-dependent width of the inversion layer.

3.3.1 Calculating the Normal Field

The magnitude of the normal field can be defined in one of two ways. The methods differ in the way each defines a vector to which the normal field is perpendicular. The first method calculates the direction of current-flow and then finds the component of the electric field normal to this *direction-of-current-flow* reference. The second assumes that in a MOSFET with a horizontal gate, the direction of flow in the channel is almost parallel to the Si-SiO2 interface. When using this *direction-of-interface* reference, the normal field is almost identical to the vertical component of the electric field. Use of the direction of current-flow is potentially more accurate, because carriers exiting the drain end of an inversion layer flow diagonally away from the interface during saturated operation [YAMA79]. While these carriers are no longer in an inversion layer, practical constraints force the inversion-layer mobility model to be used to calculate their mobility. Thus, the mobility of these carriers will be inaccurate if the simpler, direction-of-interface reference is used. The sensitivity of MOSFET performance to this inaccuracy is tested in the next chapter.

The electron current density, $\mathbf{J}_n$, is proportional to the electron concentration, n, and the electron quasi-fermi potential gradient[1], $\mathbf{F}_n$ [MULL86]:

$$\mathbf{J}_n \propto n\mathbf{F}_n \qquad (3.1)$$

The quasi-fermi potential gradient is the total carrier drving force due to both the drift and diffusion process. Because of this, the direction of current-flow can be calculated from any one of the three vectors: $\mathbf{J}_n$, $\mathbf{F}_n$, or the weighted carrier driving force, $n\mathbf{F}_n$. The current density, $\mathbf{J}_n$, is also directly proportional to the mobility, μ_n. Because the value of the mobility is not yet known, the true direction of the

---

[1]The quasi-fermi potential gradient, $\mathbf{F}_n$, is the total carrier driving force due to both drift and diffusion.

current density is also not known. Thus, $\mathbf{J}_n$ cannot be used as the reference vector. The quasi-fermi potential gradient, $\mathbf{F}_n = \nabla \Psi - \frac{1}{n}\nabla n$ is undefined when the electron concentration, n, drops to zero. It is also very sensitive to numerical noise in n as n approaches zero. This creates problems when implemented in a numerical device simulator such as CODECS. This leaves the weighted carrier driving force, $n\mathbf{F}_n$, as the only well-defined alternative. The same arguments apply to the hole current density, $\mathbf{J}_p$.

3.3.2 Normal Field and Effective Mobility

Experimental evidence indicates that the inversion-layer mobility is a unique function of an effective normal field (cf. Section 2.4.4). In other words, if two different inversion layers have surface and bulk normal fields which lead to the same effective normal field, the mobility in those two layers is the same. The mobility derived in these experiments is called the effective mobility, μ_{eff}. The effective mobility is an average of the mobilities of each of the individual electrons in the inversion layer. If it is assumed that all electrons are influenced equally by the normal field, the effective mobility is equal to the individual mobilities. This might be the case if the scattering behavior is controlled by the inversion-layer width, which is an indirect function of the normal field. However, if it is assumed that only the individual electrons occupying a localized region have the same mobility, then a local mobility, μ_{local}, should be defined as a function of position. This local mobility varies as a function of the local value of the normal field. However, the validity of this assumption is somewhat suspect. In a device simulator, it is possible for the simulated electric field to vary on a scale which is smaller than size of an individual electron. In a real device, the size of an electron imposes a fundamental limit on spatial variation. Clearly, some inaccuracy is introduced by assuming that the mobility is a function of this nonphysical, simulated normal field. There is also another difficulty that arises from the use of a locally varying mobility within the inversion layer. An expected effective mobility can be defined as the average value of the local mobility expression over the inversion layer. Under the additional assumptions that the lateral field is negligible in comparison

to the normal field and that the inversion carrier concentration is much greater than the substrate dopant concentration, the following equation for the expected effective mobility, μ_{eff}^{exp}, in terms of the local mobility, μ_{local}, can be derived [SHIN89, eq. (7b)]:

$$\mu_{eff}^{exp} = \frac{\int_{E_{\perp}^{bulk}}^{E_{\perp}^{surf}} \mu_{local}(E_{\perp})dE_{\perp}}{E_{\perp}^{surf} - E_{\perp}^{bulk}} \qquad (3.2)$$

where $E_{\perp}^{surf}$ and $E_{\perp}^{bulk}$ are the surface and bulk normal fields at the edges of a cross-section of the channel.

Unfortunately, simple local mobility expressions do not yield completely accurate expected effective mobilities. Figure 3.1 demonstrates this problem. The expected effective mobility calculated from the above equation, μ_{eff}^{exp}, is plotted versus effective normal field, $E_{\perp}^{eff}$ (cf. Equation 2.6). Each member of the family of curves in the figure corresponds to a different value of $E_{\perp}^{bulk}$. The value of $E_{\perp}^{eff}$ was varied by changing the value of the surface normal field, $E_{\perp}^{surf}$. The new CODECS local mobility expression for electrons was used for μ_{local}. As can be seen, the expected effective mobility is not a unique function of the effective normal field. Since experimental evidence indicates that a single effective mobility exists for a given effective normal field, the expected effective mobility does not exactly model this behavior. However, proper selection of local mobility model parameters can often reduce the impact of this nonideality.

3.3.3 Types of Modelling Approaches

Three approaches to modelling the normal-field dependence of the mobility are considered. The first is a nonlocal, or effective mobility, approach where a single value of the mobility is calculated as a function of properties of the entire inversion layer. This mobility is then assumed to apply to all inversion-layer carriers. A second approach is to define a locally varying mobility that depends exclusively on local properties of the inversion layer, such as field strength or carrier concentration. The third is a hybrid approach, where the mobility varies locally, but depends in part on overall properties of the inversion layer. A particularly convenient hybrid approach is

one where the nonlocal information is invariant with time, such as distance from the Si-SiO2 interface. Of these approaches, the effective mobility and hybrid mobility approaches are equally capable of producing accurate results. However, each is difficult to implement in a device simulator. In contrast, the local mobility approach is much easier to implement, but does not produce completely accurate results. In the following chapter, the specific constraints of a real device simulator are considered, and practical implementations of both local and hybrid-approach models are developed.

3.3.4 Normal-Field-Dependent Expressions

Normal-field mobility degradation has a dramatic effect on the performance of present-day MOS devices. Many expressions for the normal-field dependence have been advanced [HIRO87, PADM89, YAMA79, SCHW83, SELB85, LIAN86]. Several of them involve the assumption that the size of the electric field determines the width of the channel, which in turn limits the mean free path of the carriers. Thus, such models attempt to determine the channel width as a function of the effective normal field, and then assume that the mobility due to this mechanism is directly proportional to channel width. Sometimes these expressions involve empirically determined parameters, e.g. [SCHW83]. Other models simply match empirical expressions to data to determine the normal-field dependence [LIAN86]. Both of these methods produce a model for the effective mobility. This mobility is then combined with the field-independent mobility, often by using a Matthiessen rule of order 1. However, some implementations require the use of a local mobility expression. A good effective mobility expression is generally not useful as a local mobility expression. As previously noted, it is theoretically questionable whether or not a local mobility should be used. It is therefore impossible to derive a theoretical expression for the local mobility. Instead, empirical expressions are used for local mobility models [YAMA79]. In particular, the following local mobility expression is used to model normal-field (NF) dependence in the new inversion-layer mobility model of CODECS:

$$\mu_{NF} = \frac{\mu_0}{1 + \theta_a E_\perp + \theta_b E_\perp{}^2} \tag{3.3}$$

where μ_0, θ_a, and θ_b are all empirically determined parameters. The low field mobility, μ_0, is recognized as the field-independent mobility model parameter. The same expression can also be used for the effective mobility, provided that the parameters μ_0, θ_a, and θ_b are adjusted appropriately.

3.4 Lateral-Field-Dependent Mobility

As the strength of the lateral field increases, hot carrier scattering degrades the mobility. Hot carrier scattering is treated by defining a hot-carrier mobility, μ_{hot}, by:

$$\mu_{hot} = v_{sat}/F \tag{3.4}$$

where v_{sat} is the maximum attainable velocity, and F is the magnitude of the quasi-fermi potential gradient. The net carrier velocity is the product of the mobility and the magnitude of the quasi-fermi potential gradient: μF. If it is assumed that the overall mobility is equal to μ_{hot}, the net carrier velocity is v_{sat}. However, at low lateral fields μ_{hot} is very high, much higher than the mobility due to other scattering mechanisms. Only at high lateral fields is this mobility lower than the low-field mobility. Thus, when a Matthiesen's rule is used to combine the low-field and hot-carrier mobilities, μ_{hot} dominates at high lateral electric fields. There are two popular models which include this basic feature. The first is the Caughey-Thomas expression for the lateral-field-dependent (LF) mobility [CAUG67]:

$$\mu_{LF} = \frac{\mu_{NF}}{\left(1 + \left(\frac{\mu_{NF}E_{\parallel}}{v_{sat}}\right)^{\beta}\right)^{1/\beta}} \tag{3.5}$$

The second is the Scharfetter-Gummel expression, modified according to Thornber's scaling theory [THOR80]:

$$\mu_{LF} = \frac{\mu_{NF}}{\sqrt{1 + \frac{(\mu_{NF}E_{\parallel}/v_{ac})^2}{(\mu_{NF}E_{\parallel}/v_{ac})+A} + \left(\frac{\mu_{NF}E_{\parallel}}{v_{sat}}\right)^2}} \tag{3.6}$$

In both these expressions the magnitude of the quasi-fermi potential gradient has been replaced by the lateral field strength, $E_{\parallel}$, which is approximately equivalent

in critical regions of a MOSFET. Deciding which field to use to calculate velocity saturation is an interesting problem. There are at least three available alternatives. The first is the magnitude of the quasi-fermi potential gradient, F, which is always in the exact direction of current-flow. This quantity is preferred because it represents the total driving force due to both drift and diffusion. Unfortunately, it has already been noted that F behaves poorly as it approaches zero, and so complicates any implementation based on it. The second is the component of electric field in the direction of current flow, the lateral field. Third, because in a typical MOSFET the channel current is almost parallel to the direction of the gate and Si-SiO2 interface, another alternative is available. This is the component of the field in the direction of the interface. Either of the final two alternatives can be considered in a device simulator such as CODECS.

Chapter 4

The CODECS Inversion-Layer Mobility Model

4.1 Summary

Chapter 3 reviews methods for modelling the inversion-layer mobility. However, some of these methods cannot be easily implemented in every device simulator. Therefore, an inversion-layer mobility model must be tailored to the specific constraints of a device simulator. In this chapter, the implementation of a new mobility model into the CODECS device simulator, DSIM, is presented. An overview of DSIM can be found in Appendix C. Here, focus is maintained on the inversion-layer mobility model and its relationships to the various elements of the device simulator.

A summary of the DSIM device simulator is presented to highlight the role of the mobility in the overall simulation task. Methods used to model the normal-field dependence of the mobility are considered in terms of their impact on the Jacobian matrix of the equations for DC analysis. Based on these considerations, both the local mobility approach and a hybrid mobility approach are feasible alternatives for the new inversion-layer mobility model. For each of these approaches, the expressions used to calculate the electron and hole inversion-layer mobilities are shown.

The new mobility expressions are both normal and lateral-field dependent. Estimates for these two components of the electric field are obtained for all relevant

20

regions of a semiconductor device. Next, the new mobility model is integrated into the DC analysis algorithms of DSIM. Because device simulation is already computation-intensive, several alternatives for reducing the additional computational burden imposed by the model have been tested. Selection or rejection of each of these alternatives is linked to acceptable convergence behavior of the DC algorithms.

4.2   Summary of the DSIM Device Simulator

DSIM is based on the solution of Poisson's equation and the electron and hole current-continuity equations. Solution of these equations provides the electric potential, Ψ, and the electron and hole concentrations, n and p. The continuous domain of a real device is approximated in DSIM by a finite rectangular simulation mesh, as shown in Figure 4.1. Important dimensions of the mesh are identified in Figure 4.2. The unknown quantities, Ψ, n, and p, are approximated at the nodes of this mesh. The current density and electric field are calculated at the midpoints of the edges of the mesh. Values for the electron and hole mobilities, μ_n and μ_p, must be determined for each silicon edge of the mesh in order to calculate the current densities. The following notation is used for referring to various quantities, u and Δu, in terms of the column and row indices of the mesh, i and j:

$$
\begin{aligned}
u_{i,j} &\equiv u(x_i, y_j) \\
u_{i+\frac{1}{2},j} &\equiv u\left(\frac{x_{i+1} + x_i}{2}, y_j\right) \\
u_{i,j+\frac{1}{2}} &\equiv u\left(x_i, \frac{y_{j+1} + y_j}{2}\right) \\
\Delta u_{i+\frac{1}{2},j} &\equiv u_{i+1,j} - u_{i,j} \\
\Delta u_{i,j+\frac{1}{2}} &\equiv u_{,j+1} - u_{i,j}
\end{aligned}
$$

For example, the potential at node (i, j) in Figure 4.2 is denoted $\Psi_{i,j}$, and the electron mobility at the center of the edge to the right of that node is denoted $\mu_n|_{i+\frac{1}{2},j}$.

4.3   Choosing a Normal-Field Dependence

Section 3.3.3 presents three different approaches to the problem of modelling the normal-field dependence of the mobility. Each of these approaches does its best to match effective mobility curves such as those of [WATT87] in Section 2.4.4.

The way each method uses the normal fields in an inversion layer to calculate the mobility distinguishes one method from another. Figure 4.3 shows how each approach would be used to calculate the mobilities for a vertical cross-section of inversion-layer edges. The first and most accurate approach, shown in Figure 4.3a, directly computes the effective normal field, $E_\perp^{eff}$, from $E_\perp^{surf}$ and $E_\perp^{bulk}$ at a particular horizontal location. This field is used in an expression for the effective mobility, and the effective mobility is used throughout the vertical cross-section of the inversion layer. A second approach is to define a local normal field, $E_\perp^{local}$, at the midpoint of each individual edge. A representative edge has been selected in Figure 4.3b. Each local field can then be used in a local mobility expression to find the mobility for one edge. The drawback to this approach is that the effective mobility of the inversion layer is no longer a unique function of the effective normal field (cf. Section 3.3.2). The third approach uses a hybrid mobility expression. Two different hybrid expressions are derived in Appendix D. The first expression depends on both the local normal field, $E_\perp^{local}$, and the bulk normal field, $E_\perp^{bulk}$, as shown in Figure 4.3c. The second expression uses the surface normal field, $E_\perp^{surf}$, instead of $E_\perp^{bulk}$, as shown in Figure 4.3d. The global information about $E_\perp^{bulk}$ or $E_\perp^{surf}$ is used to compensate for the nonuniqueness deficency of the purely local approach. Thus, the hybrid mobility is different for each edge of the cross-section, but the overall effective mobility is correctly computed.

As noted in Appendix C, the DC analysis algorithms of DSIM solve a set of equations, $F(u)$, for a set of unknowns, u, using an iterative method which employs the Jacobian matrix of those equations. The $(i,j)^{th}$ entry of the Jacobian is the partial derivative of the ith equation, F_i, with respect to the jth unknown, u_j. In DSIM, if field-independent mobilities are used, each equation is a function of a limited set of unknowns, and many of these partial derivatives are zero all the time. However, field-dependent mobilities increase the set of unknowns on which the discretized current-

continuity equations depend, and consequently the number of nonzero entries, or size, of the Jacobian. Each discretized current-continuity equation uses estimates of the local current density. The current density is proportional to the mobility, the mobility is dependent on the normal field, and the normal field is dependent on estimated values of the electric potential. The unknown electric potential values that are used to calculate the normal field are responsible for part of the increase in the size of the Jacobian. Some of these values are not used in the current-continuity equations when constant, field-independent mobilities are used.

Mobilities that are functions of nonlocal normal fields have negative effects on the size and continuity of the Jacobian. Dependence on the surface normal field, $E_\perp^{surf}$, as in the effective mobility approach, is not a serious problem because the set of unknowns used to calculate $E_\perp^{surf}$ does not change. Thus, the size of the Jacobian is only increased in order to account for this fixed set of unknowns. However, dependence on the bulk normal field, $E_\perp^{bulk}$, is highly problematic because the location of the bulk edge of the inversion layer changes as the applied biases on a MOSFET change. The bulk normal field is computed from estimates of the electric potential near the bulk edge of the inversion layer. If the position of the bulk edge changes, the unknowns used to calculate $E_\perp^{bulk}$ also change. Many mesh edges and unknowns are generally needed to accurately approximate the varying inversion layer. The possibility that one of these unknowns may contribute to $E_\perp^{bulk}$ at some time implies that the derivative of $E_\perp^{bulk}$ with respect to that unknown is not always zero. Thus, $E_\perp^{bulk}$-dependent mobilities cause the number of nonzero entries in the Jacobian to explode. Even more troubling is the fact that the set of unknowns used to compute $E_\perp^{bulk}$ changes. In one situation, $E_\perp^{bulk}$ may use the value of a particular unknown, while in another, that same unknown may not be needed at all. This conditional dependence creates discontinuities in some of the derivatives which make up the Jacobian. It is well known that a discontinuous Jacobian matrix can lead to nonconvergence of the iterative algorithm. Other authors who have tried the bulk-field-dependent hybrid approach have reported convergence difficulties, although they did not pinpoint the source of these difficulties [SHIN89]. In light of these problems, no method which uses $E_\perp^{bulk}$ can be implemented in DSIM.

The local mobility approach, which depends only upon the local normal field, $E_\perp^{local}$, does not suffer from these problems. Calculation of $E_\perp^{local}$ involves a fixed and reasonably limited set of unknowns and only slightly increases the number of nonzero entries in the Jacobian matrix. The hybrid mobility approach which uses an $E_\perp^{local}$-and-$E_\perp^{surf}$-dependent expression is also acceptable. The ability of this approach to accurately compute the effective mobility makes it especially attractive. Unfortunately, it is more difficult to implement in DSIM, and the Jacobian is larger because of the dependence on two field estimates instead of just one. Based on these considerations, both the local mobility approach and the surface-field-dependent hybrid approach have been implemented. The accuracies of the two resulting models are tested in the following chapter, and a comparison of the results is used to determine which model is more suitable for MOSFET simulations.

4.4   Form of the Inversion-Layer Mobility Model

An initial constant parameter, μ_{LV}, is used to characterize the effect of lattice vibration (LV) scattering. This is then modified by an expression measuring the surface roughness (SR) dependence and the low-lateral-field mobility, μ_{SR}, is obtained. Next, μ_{SR} is further modified by an expression for hot-carrier (HC) scattering which includes the effect of velocity saturation. Equations 4.1 reflect this form for the new inversion-layer mobility model in DSIM:

$$\begin{aligned}
\mu_{LV} &= \mu_0 \\
\mu_{SR} &= f(\mu_{LV}, E_\perp) \\
\mu_{HC} &= g(\mu_{SR}, E_\parallel)
\end{aligned} \tag{4.1}$$

The final result, μ_{HC}, is used for all edges where an inversion layer may be present. This set of edges is identified by the user as part of the input specification of a simulation. The original DSIM bulk mobility expressions are used for all other edges of the simulation mesh.

As described in the previous section, the normal field dependence, quantifying surface roughness scattering, uses a local mobility approach. The local mobility

expression is chosen so that the computed effective mobility is as accurate as possible. There are many different expressions in the literature available for consideration (cf. 3.3.4). However, it is often difficult to determine whether an equation is meant to be an effective mobility expression or a local mobility expression. Because of this, the following empirical expression has been explicitly developed for use as a local mobility expression in DSIM:

$$\mu_{SR} = \frac{\mu_{LV}}{1 + \theta_a E_\perp + \theta_b E_\perp{}^2} \qquad (4.2)$$

where different parameters are used for electrons, n, and holes, (p):

$$
\begin{aligned}
\mu_{LV}^{n(p)} &= 991\ (240)\ cm^2/Vs \\
\theta_a^{n(p)} &= 2.67 \times 10^{-6}\ (2.4 \times 10^{-6})\ cm/V \\
\theta_b^{n(p)} &= 4.18 \times 10^{-14}\ (0.0)\ (cm/V)^2
\end{aligned}
$$

This expression is also used for the effective mobility in the hybrid-mobility approach. All of the parameter values are the same, except for the value of $\theta_a^{(p)}$, which is increased to $3.07 \times 10^{-6}\ cm/V$. For electrons, the fitting parameters: μ_{LV}, θ_a, and θ_b, were determined by a least-squares fit to an effective mobility curve derived from the data of [WATT87]. For holes, this same approach yielded an unacceptable negative value for θ_b, and a trial-and-error method was used instead. Because the local mobility approach introduces some error into the effective mobility, some adjustment of the parameters is usually necessary to produce better results for a specific MOSFET.

The lateral-field dependence models the effects of hot carrier scattering. DSIM originally supplied two expressions for velocity saturation in its bulk mobility model. Two similar expressions are provided for the inversion-layer mobility models. The first, which is implemented in both the local and hybrid approaches, is the Caughey-Thomas expression [CAUG67]:

$$\mu_{HC} = \frac{\mu_{SR}}{\left(1 + \left(\frac{\mu_{SR} E_\parallel}{v_{sat}}\right)^\beta\right)^{1/\beta}} \qquad (4.3)$$

where

$$\beta^{n(p)} = 2.0\ (1.0)$$

$$v_{sat}^{n(p)} = 1.1 \times 10^7 \, (9.5 \times 10^6) \, cm/s$$

The second, available only in the local mobility approach, is the Scharfetter-Gummel expression, as modified according to the Thornber mobility-scaling theory [THOR80]:

$$\mu_{HC} = \frac{\mu_{SR}}{\sqrt{1 + \frac{(\mu_{SR}E_{\parallel}/v_{ac})^2}{(\mu_{SR}E_{\parallel}/v_{ac})+A} + \left(\frac{\mu_{SR}E_{\parallel}}{v_{sat}}\right)^2}} \qquad (4.4)$$

where

$$A^{n(p)} = 8.8 \, (1.6)$$

$$v_{ac}^{n(p)} = 4.9 \times 10^6 \, (2.9 \times 10^6) \, cm/s$$

$$v_{sat}^{n(p)} = 1.04 \times 10^7 \, (1.2 \times 10^7) \, cm/s$$

This expression is only slightly different from the lateral-field dependence of the original Scharfetter-Gummel equation [SCHA69].

4.5 Calculation of Normal and Lateral Electric Fields

Estimates of the normal and lateral components of the electric field must be computed at the center of each silicon edge of the simulation mesh. First, local values of the electric field, E, and, if necessary, the weighted carrier driving force, nF_n, are calculated. The electric field components, $E_\perp$ and $E_\parallel$, are then defined in relation to one of the two available coordinate references. The *direction-of-current-flow* reference and the *direction-of-interface* reference are introduced in Section 3.3.1.

4.5.1 Finding the Electric Field and Driving Forces

Every edge in the simulation mesh is joined to two neighboring rectangular regions known as elements. Each element represents a region of one of four different types of materials: silicon, oxide, metal, or imaginary space. Imaginary space is a

convenient name for areas lying beyond the the artificial boundaries of a device. The current density is only needed for edges bordered on at least one side by a silicon element. Figure 4.4 shows the four representative cases where a horizontal edge is bounded from beneath by a silicon element. Similar cases exist for edges bounded from above by silicon and for vertical edges. The upper nodes and edges have been removed from the imaginary space and metal cases because it is unnecessary to compute the solution in those regions.

In each case, the following equations can be used to find the X components of the electric field and weighted carrier driving forces (cf. Section C.3):

$$E_x|_{i+\frac{1}{2},j} = -\frac{\Delta\Psi_{i+\frac{1}{2},j}}{\Delta x_{i+\frac{1}{2}}} \tag{4.5}$$

$$nF_{nx}|_{i+\frac{1}{2},j} = \frac{\left[n_{i+1,j}B(\Delta\Psi_{i+\frac{1}{2},j}) - n_{i,j}B(-\Delta\Psi_{i+\frac{1}{2},j})\right]}{\Delta x_{i+\frac{1}{2}}} \tag{4.6}$$

$$pF_{px}|_{i+\frac{1}{2},j} = \frac{\left[p_{i,j}B(\Delta\Psi_{i+\frac{1}{2},j}) - p_{i+1,j}B(-\Delta\Psi_{i+\frac{1}{2},j})\right]}{\Delta x_{i+\frac{1}{2}}} \tag{4.7}$$

where $B(x) = \frac{x}{e^x-1}$ is the Bernoulli function, and $\Delta\Psi_{i+\frac{1}{2},j} = \Psi_{i+1,j} - \Psi_{i,j}$. The Y components must be determined through separate consideration of each case.

Figure 4.4a shows the case when an edge is situated between two silicon elements. A local potential function which varies linearly in the X direction and quadratically in the Y direction can be constructed based on discrete estimates of the potential near the edge. It is assumed that this function is a good approximation for the actual potential, and that the negative gradient of this function approximates the electric field. Then it can be shown that the Y component of the electric field at the midpoint of the edge is estimated by:

$$E_y|_{i+\frac{1}{2},j} = \frac{\Delta y_{j+\frac{1}{2}}}{\Delta y_{j+\frac{1}{2}} + \Delta y_{j-\frac{1}{2}}}E_y|_{i+\frac{1}{2},j-\frac{1}{2}} + \frac{\Delta y_{j-\frac{1}{2}}}{\Delta y_{j+\frac{1}{2}} + \Delta y_{j-\frac{1}{2}}}E_y|_{i+\frac{1}{2},j+\frac{1}{2}} \tag{4.8}$$

where

$$E_y|_{i+\frac{1}{2},j-\frac{1}{2}} = \frac{E_y|_{i,j-\frac{1}{2}} + E_y|_{i+1,j-\frac{1}{2}}}{2}$$

$$E_y|_{i+\frac{1}{2},j+\frac{1}{2}} = \frac{E_y|_{i,j+\frac{1}{2}} + E_y|_{i+1,j+\frac{1}{2}}}{2}$$

The individual field estimates, E_y, are each computed using an appropriate finite difference formula. While it is not strictly valid to make the same assumptions about the driving force, similar equations are used to estimate nF_{ny} and pF_{py} by replacing field estimates with driving force estimates in the above equation.

In Figure 4.4b, the edge lies between silicon and oxide elements, and thus is part of the Si-SiO2 interface. It is somewhat difficult to compute the value of the Y component of the field for such edges. It is inappropriate to use the same method as for silicon-silicon edges, because the electric field is not continuous across the interface boundary. Because the field often varies rapidly on the silicon side, only a crude estimate for this component is obtained by averaging the two vertical estimates for the electric field on the silicon side. A better estimate can be obtained by averaging the electric field on the oxide side:

$$E_y|_{i+\frac{1}{2},j} = \frac{E_y|_{i,j+\frac{1}{2}} + E_y|_{i+1,j+\frac{1}{2}}}{2} \tag{4.9}$$

This estimate is better because the electric field does not vary within the oxide above the edge. In the absence of fixed charge at the interface, the silicon field is then related to the oxide field by the following:

$$E_y|_{silicon} = \epsilon_{rel} E_y|_{oxide} \tag{4.10}$$

where $\epsilon_{rel} = \epsilon_{ox}/\epsilon_{si}$ is the ratio of the dielectric constants of the two materials. Because no current can flow from the silicon into the oxide, the Y components of the driving forces are zero.

When the edge is part of the artificial boundary of a device, as in Figure 4.4c, boundary conditions on this type of interface guarantee that the Y components of both the field and the driving forces are identically zero. Finally, for edges between silicon and a metal contact, there is never a potential difference across the edge because of the contact. No current ever flows, and the value of the mobility is irrelevant. Thus, there is no need to compute the Y components of the field and driving forces, even though they are not identically zero.

4.5.2   Computing the Normal and Lateral Fields

Once the electric field and weighted carrier driving forces are known, $E_\perp$ and $E_\parallel$ can be determined. With a direction-of-interface reference, the following set of equations can be used for horizontal interfaces:

$$E_\perp = |E_y| \tag{4.11}$$

$$E_\parallel = |E_x| \tag{4.12}$$

and this set can be used for vertical interfaces:

$$E_\perp = |E_x| \tag{4.13}$$

$$E_\parallel = |E_y| \tag{4.14}$$

If the direction-of-current-flow reference is used, the following equations are applicable for electrons [YAMA79]:

$$E_\perp = \left| \mathbf{E} \times n\hat{\mathbf{F}}_n \right| \tag{4.15}$$

$$E_\parallel = \left| \mathbf{E} \cdot n\hat{\mathbf{F}}_n \right| \tag{4.16}$$

where

$$n\hat{\mathbf{F}}_n = \frac{n\mathbf{F}_n}{|n\mathbf{F}_n|} = \frac{n\mathbf{F}_n}{\sqrt{(n\mathbf{F}_{nx})^2 + (n\mathbf{F}_{ny})^2}} \tag{4.17}$$

The equations for holes can be found by replacing $n\mathbf{F}_n$ with $p\mathbf{F}_p$.

This approach presents a serious difficulty when $|n\mathbf{F}_n|$ equals zero. In this case, $n\hat{\mathbf{F}}_n$ is undefined, as are $E_\perp$ and $E_\parallel$. In addition, for $|n\mathbf{F}_n|$ very small, the derivatives of the mobility with respect to the weighted carrier driving force components become very large. This discontinuity can prevent the Newton iteration from converging. An attempt to correct this problem has been made by using a different expression to compute $|n\mathbf{F}_n|$:

$$|n\mathbf{F}_n| = \sqrt{(n\mathbf{F}_{nx})^2 + (n\mathbf{F}_{ny})^2 + (n\mathbf{F}_{nz})^2} \tag{4.18}$$

where $n\mathbf{F}_{nz}$ is an artificially introduced parameter which prevents $|n\mathbf{F}_n|$ from going to zero. This corrupts the calculation of the electric field components for driving forces in the neighborhood of $n\mathbf{F}_{nz}$. The value of $n\mathbf{F}_{nz}$ must therefore be lower than any driving force levels of interest but still high enough to avoid convergence difficulties.

4.5.3 Field Components and the Jacobian

When computing the Jacobian of the DC analysis equations, the derivatives of the mobility with respect to the unknown potential and carrier concentrations, $\frac{\partial \mu}{\partial w}$, must be calculated. Values of the unknowns are used to find the electric field and weighted carrier driving force. The functional dependence of the mobility on the X and Y components of the electric field and driving force can be expressed as:

$$\mu = \mu(\ E_\perp(\ E_x, E_y, nF_{nx}, nF_{ny} \ ), \ E_\parallel(\ E_x, E_y, nF_{nx}, nF_{ny} \ ) \ ) \tag{4.19}$$

This representation can be used for any of the three relationships which define $E_\perp$ and $E_\parallel$. By taking the total derivative of this equation with respect to an unknown, the following formula for $\frac{\partial \mu}{\partial w}$ is obtained:

$$\frac{\partial \mu}{\partial w} = \left(\frac{\partial \mu}{\partial E_x} \right) \frac{\partial E_x}{\partial w} + \left(\frac{\partial \mu}{\partial E_y} \right) \frac{\partial E_y}{\partial w} + \left(\frac{\partial \mu}{\partial nF_{nx}} \right) \frac{\partial nF_{nx}}{\partial w} + \left(\frac{\partial \mu}{\partial nF_{ny}} \right) \frac{\partial nF_{ny}}{\partial w} \tag{4.20}$$

where w is one of the unknowns used to compute the field or driving force. If a direction-of-interface reference is used to define $E_\perp$ and $E_\parallel$, the mobility is independent of the driving force, and the driving force derivatives, $\frac{\partial \mu}{\partial nF_{nx}}$ and $\frac{\partial \mu}{\partial nF_{ny}}$, are always zero.

The above equation for $\frac{\partial \mu}{\partial w}$ uses the total derivatives of the mobility with respect to the field and driving force components. These derivatives are calculated by combining separate contributions due to $E_\perp$ and $E_\parallel$. One of these computations is shown below:

$$\frac{\partial \mu}{\partial E_x} = \left(\frac{\partial \mu}{\partial E_\perp} \right) \frac{\partial E_\perp}{\partial E_x} + \left(\frac{\partial \mu}{\partial E_\parallel} \right) \frac{\partial E_\parallel}{\partial E_x} \tag{4.21}$$

where the appropriate relationship for $E_\perp$ and $E_\parallel$ is used to define the derivatives $\frac{\partial E_\perp}{\partial E_x}$ and $\frac{\partial E_\parallel}{\partial E_x}$. Auxiliary expressions derived from the mobility equations are used to compute the derivatives of the mobility with respect to the normal and lateral fields, $\frac{\partial \mu}{\partial E_\perp}$ and $\frac{\partial \mu}{\partial E_\parallel}$. The interested reader can find these expressions in Appendix A.

4.6   Results on Convergence of Methods

4.6.1   Decision to Compute Accurate Jacobian

Because of the large amount of time used in calculating the accurate Jacobian when field-dependent mobilities are in use, some authors have suggested using a different iteration matrix, $\tilde{J}(\mathbf{u})$, which approximates the accurate $J(\mathbf{u})$ [FRAN83]. One particularly appealing choice for $\tilde{J}(\mathbf{u})$ is the Jacobian that results if the calculated mobilities are assumed to be independent of the normal and lateral electric fields. In other words, the mobility derivative terms are simply ignored. Unfortunately, there is no theoretical basis which can guarantee the convergence of the resulting quasi-Newtonian method. Experiments using this approximate Jacobian, $\tilde{J}(\mathbf{u})$, show that reliable convergence cannot be achieved when simulating MOSFETS in either the linear or saturation regions of operation. As a result of these experiments, DSIM computes the complete and accurate Jacobian.

4.6.2   Choice of Reference for Normal-Lateral Calculations

Two different coordinate references for computing the normal and lateral electric field components have been presented: the direction of current-flow and the direction of the interface. The convergence performances of these coordinate systems were compared. The MOSFET shown in Figure 4.5 has been simulated in both the linear and saturation regions of operation. Figures 4.6a,b show the drain current, I_{DS}, versus gate voltage, V_{GS}, for these two cases, respectively. The nonlinear behavior of the linear-region drain current is indicative of normal-field mobility degradation. As can be seen from the figure, the two methods produce identical results. However, the simulations employing the direction-of-current-flow reference took slightly longer to complete, because the normal and lateral-field calculations are more complicated. For this reason, the simpler direction-of-interface reference is marginally preferrable.

4.6.3 Changes to DC Transfer Curve Initial Guess Scheme

During a DC transfer curve analysis, CODECS uses a linear interpolation scheme to establish initial guesses, u^0. This method uses the Jacobian as well as the derivatives of the equations $F(u)$ with respect to applied biases. Field-dependent mobilities affect the Jacobian and the bias-dependent derivatives. Convergence can generally be achieved if new terms in the bias-dependent derivatives are ignored. However, including them decreases iteration count because the initial guess is closer to the final solution.

Chapter 5

Verification of Model Accuracy

5.1 Summary

Two new inversion-layer mobility models have been implemented in DSIM. They differ in the way they treat normal-field dependence of the mobility. One is based on the simpler local-mobility approach, whereas the other relies on the more complex surface-field-dependent hybrid-mobility approach. These models bring together a variety of theoretical and experimental work in their design. Because a number of assumptions are involved in this synthesis, the accuracies of the overall models need to be established. From a device physicist's point of view, the models can be tested in terms of their dependencies on the normal and lateral fields. In contrast, a circuit designer is more interested in the accuracy of MOSFET drain-current simulations. Ideally, the models should be tested from both points of view. In this chapter, the normal-field dependencies of the inversion-layer mobility models are tested by comparison of simulations to experimental data. Attention has been restricted to the normal-field dependence because it is the major new feature in the DSIM mobility model. This is a reasonable first step in the verification of model accuracy.

When a MOSFET is operated in the ohmic region and the drain-to-source voltage, V_{DS}, is made very small, the channel is almost uniform along its length. As a result, the drain current, I_{DS}, is almost directly proportional to V_{DS}. It is also directly

proportional to the effective mobility, μ_{eff}, in this *linear* region. Experiments which extract the effective mobility from drain-current simulations of MOSFET's in this region have been performed. The results are compared to the mobility-field curves of Watt and Plummer [WATT87]. Comparison shows that simulations with the new models are substantially more accurate than those using the original DSIM mobility model, which is better suited to use as a bulk mobility model. Simulation of the drain current in the linear region will be correspondingly improved. However, the two new models do not perform equivalently; the hybrid-approach model is more accurate than the local-approach model. Various nonidealities in the local-approach model make the simulated mobility deviate slightly but significantly from the experimentally determined mobility. The nonidealities affect the mobility of holes more than the mobility of electrons. The importance of this deviation is dependent upon the specific circumstances of an application. In contrast, the hybrid-approach model provides consistently accurate results, and thus is preferrable to the local-approach model.

From a circuit designer's point of view, the models should also be tested by examining drain-current simulations in the three major regions of MOSFET operation: the subthreshold, ohmic, and saturation regions. The models have been checked in the linear region, which is a subset of the ohmic region. However, more extensive testing needs to be performed under a greater variety of bias conditions. For example, in the nonlinear-ohmic and saturation regions, the normal field varies along the length of the channel. Whether or not the mobility varies appropriately under these conditions has not been verified. In addition, in a saturated short-channel MOSFET, carriers may experience velocity saturation, due to large lateral fields, along much of the length of the channel. Experiments with these devices would indirectly test the lateral-field dependence of the new models.

5.2 Measurement of Effective Mobility

In this section the procedures for extracting the effective mobility and the surface and bulk normal electric fields from the results of a CODECS simulation are described. These procedures are contrasted with those used by Watt and Plummer

to extract the mobility from experimental data. Although the following derivation focuses on electron inversion layers, analogous arguments apply to holes.

A MOSFET with a very long channel length, L, and reasonable width, W, is shown in Figure 5.1. The width and length of the device are chosen to minimize various undesired edge effects. In addition, the long channel contributes to the formation of a quasi-uniform inversion layer. If the drain-to-source voltage, V_{DS}, is made small, the lateral electric field, $E_\parallel \approx V_{DS}/L$, is uniform and very small over the entire channel. The magnitude of the drain-current per unit width, $|J_{DS}|$, in a uniform NMOS inversion layer can be expressed as an integral across the thickness of the inversion layer:

$$|J_{DS}| = \int_{y^{bulk}}^{y^{surf}} q\mu(y)n(y)E_\parallel dy \qquad (5.1)$$

where y^{surf} and y^{bulk} are the locations of the surface and bulk edges of the inversion layer. It can also be written in terms of the effective electron mobility, μ_{eff}^n, and the total inversion-layer charge, qN_{inv}:

$$|J_{DS}| = q\mu_{eff}^n N_{inv} E_\parallel \qquad (5.2)$$

Combination of these two expressions and the fact that $N_{inv} = \int_{y^{bulk}}^{y^{surf}} n(y)dy$ leads to the following expression for μ_{eff}^n:

$$\mu_{eff}^n = \frac{|J_{DS}|}{qN_{inv}E_\parallel} = \frac{\int_{y^{bulk}}^{y^{surf}} \mu(y)n(y)dy}{\int_{y^{bulk}}^{y^{surf}} n(y)dy} \qquad (5.3)$$

Because DSIM uses a finite simulation grid, the integrals in the above expression must be replaced by sums over the inverted region of the grid. Figure 5.2 shows the basic structure of the grid in the vicinity of the interface. At each horizontal edge, estimates of the current density in the lateral direction, J_i, and the local mobility, μ_i, are available. These values can be used to compute the effective mobility as:

$$\mu_{eff}^n = \frac{\sum_{i\in I} J_i \Delta y_i}{\sum_{i\in I} \frac{J_i}{\mu_i} \Delta y_i} \qquad (5.4)$$

where the set I contains a vertically aligned set of horizontal edges within the inversion layer. The set I is terminated at the last edge where the inversion carrier

concentration is greater than the substrate dopant concentration. This formula is functionally equivalent to a direct discretization of the expression which contains the integrals.

Watt and Plummer use an expression related to Equation 5.2 to calculate the effective mobility from measurements of the drain conductance, g_{DS}:

$$\mu_{eff}^n = \left.\frac{g_{DS}}{(W/L)qN_{inv}}\right|_{V_{DS}=0} \tag{5.5}$$

The inversion-layer charge, qN_{inv}, is estimated using analytical expressions.

The effective mobility is plotted as a function of the effective normal field for an inversion layer. The effective normal field, $E_{\perp}^{eff}$, is defined as:

$$E_{\perp}^{eff} = \alpha E_{\perp}^{bulk} + \beta E_{\perp}^{surf} \tag{5.6}$$

The parameters α, β have been determined empirically to be $\frac{1}{2}, \frac{1}{2}$ for electrons and $\frac{2}{3}, \frac{1}{3}$ for holes. An alternative form expressed in terms of the total inversion-layer charge, Q_{inv}, and total depletion-layer charge, Q_{depl}, is used in the Watt-Plummer experiments:

$$E_{\perp}^{eff} = \frac{1}{\epsilon_{si}}(Q_{depl} + \beta Q_{inv}) \tag{5.7}$$

where β is the same as in the above equation. Under the assumption that the inversion-layer width is negligibly small compared to the depletion-layer width, the two forms can be related to each other using Gauss's law.

The surface and bulk normal fields must be calculated from the results of DSIM simulations. The surface normal field is estimated using Equation 4.9. An estimate for the bulk normal field is obtained from one of the vertical edges connecting the last inversion-layer horizontal edge to the first non-inverted edge, as shown in Figure 5.2.

5.3 Experimental Design

MOSFET's similar to the ones used in the experiments of Watt and Plummer were simulated. Each device has a gate oxide thickness, T_{ox}, of 875Å and a W/L of

$50\mu/50\mu$. The substrate dopant concentration was varied between $3.0 \times 10^{14}/cm^3$ and $2.0 \times 10^{17}/cm^3$. Both NMOS and PMOS devices were simulated in order to verify the mobility models for electrons and holes, respectively. In addition, the simulations were performed using both the local-approach mobility model and the hybrid-approach mobility model.

Accurate results rely on a close approximation of discrete sums to continuous integrals when computing the effective mobility. This forces careful attention to the structure of the finite simulation grid near the interface. Starting at the interface, twelve rows of grid points are placed in the silicon within a distance of one extrinsic Debye length[1] from the interface. The extrinsic Debye length is characteristic of spatial variations of the potential and is a useful approximation to the width of the inversion layer. The spacing of the rows is nonuniform; rows nearer to the interface are closer together than rows farther away[2]. In other regions of the device, such as near the source and drain edges, normal simulation mesh is used.

The drain-to-source voltage, V_{DS}, is set at 1V for NMOS devices and -1V for PMOS devices. The gate-to-source voltage, V_{GS}, is then swept from a magnitude of 0V to 50V at 1V intervals, to produce a varying effective normal field. The substrate bias, V_{BS}, is fixed at 0V. At each bias point, μ_{eff}, $E_{\perp}^{surf}$, and $E_{\perp}^{bulk}$ are computed at the center of the MOSFET channel.

---

[1]The *extrinsic Debye length*, L_D, is defined as [MULL86]:

$$L_D = \left[\frac{\epsilon_{si}\phi_t}{qN_{sub}}\right]^{1/2}$$

where ϵ_{si} is the dielectric constant of silicon, $\phi_t \equiv \frac{kT}{q}$ is the thermal voltage, q is the electron charge, and N_{sub} is the substrate doping concentration. For $N_{sub} = 2.3e16/cm^3$, L_D is 270Å at room temperature.

[2]The distance, d_i, between the interface and the ith row away from the interface is given by:

$$d_i = d_1 \left(\frac{L_D}{d_1}\right)^{\frac{i-1}{n-1}}$$

where L_D is the extrinsic Debye length, d_1 is the initial spacing of 1Å, and $n = 11$ is the total number of rows. The final distance, d_{11}, is L_D.

5.4 Commentary

Plots of the simulated local-approach effective mobility versus effective normal field are shown in Figures 5.3 and 5.4 for electrons and holes, respectively. Curves taken from the data of Watt and Plummer are also shown on these plots[3]. Alternatively, Figures 5.5 and 5.6 show the electron and hole hybrid-approach effective mobilities.

The families of effective electron mobility curves are plotted in Figures 5.3 and 5.5. Each member of these families begins at a different value of the effective normal field. This value is dependent on the substrate doping concentration. Overall, the sets of simulated curves follow the experimental curve quite well. In particular, the hybrid-approach mobility closely follows a single, smooth effective-mobility curve. It should be recognized that the original CODECS mobility model results in an effective mobility that is constant, independent of the effective normal field. This appears as a horizontal line on the figures. It is clear that no single value can approximate the mobility over the entire range of effective normal field. Therefore, it is reasonable to conclude that the new mobility models will improve the quality of simulations of NMOS devices in the linear region. In addition, the hybrid-approach model will be noticeably more consistent than the local-approach model.

In Figure 5.3, the local-approach mobility shows significant deviation from the experimental curve. For each device, at larger values of the effective field, the simulated effective mobility is higher than the experimental effective mobility. In Section 3.3.2, an equation is derived for the expected effective mobility. This equation can be used with the DSIM normal-field-dependent electron mobility expression to predict the outcome of the DSIM simulations. When this is done, the expected effective mobilities are actually somewhat higher than the simulated mobilities. It is believed that this effect is due to inaccuracy in the discrete computation of the simulated effective mobility.

---

[3]Because their actual data was not available, the curves were produced by measuring from figures published in their paper [WATT87]. Limitations on the accuracy of the measurement procedure cause these curves to be discontinuous. For purposes of comparison, Figure 2.3 shows that their effective electron mobility curves are quite smooth. The hole mobility curves are smooth as well.

At lower values of the effective field for each device, the effective field is dominated by the bulk normal field. In these cases, the electron effective mobility follows the local mobility expression closely. Since the local mobility expression was fit to effective mobility data, the simulated mobility follows the experimental mobility. This is a consequence of the values of α and β used in the expression for the electron effective field. However, the values of α and β are fixed by experimental results. Hence, this desirable result is unfortunately a chance circumstance.

In Figures 5.4 and 5.6, the simulated hole mobility curves also follow the experimental data reasonably well. Once again, the hybrid-approach model provides superior results. When using the local-approach model, the overall fit is not nearly as good as in the case of electrons. In particular, for each device the simulated mobility deviates significantly from the experimental data at lower values of the effective field. This result is directly related to the different values of α and β that must be used in the expression for the hole effective field. Nevertheless, both hole mobility models are substantially better than the original CODECS mobility model, which results once again in a flat mobility-versus-effective-field curve.

Chapter 6

Conclusions

Inversion-layer mobility in MOS transistor channels has been investigated in order to improve its modelling in the CODECS mixed-level circuit and device simulator. Several scattering mechanisms which affect the mobility have been reviewed. Lattice vibration scattering imposes an upper limit on the inversion-layer mobility. The mobility is largely independent from ionized impurity scattering at low to medium levels of substrate doping. At higher doping levels, impurity scattering limits the maximum attainable mobility. Electric fields normal to the direction of current flow in the inversion layer are associated with significant degradation of the mobility. Surface roughness scattering is one source of this degradation. High electric fields in the direction of current flow increase the energies of a mobile carriers appreciably above their ambient levels. These *hot carriers* are scattered effectively, and the maximum drift velocity of such carriers is limited.

The inversion-layer mobility can be modelled by its dependencies on the normal and lateral components of the electric field in the channel. The normal-field dependence should reflect the experimental evidence that the effective mobility is a unique function of an effective, or average, normal field within the inversion layer. Many theoretically grounded expressions for this dependence have already been advanced, but a simple, yet flexible, empirical relation can yield adequate results. The lateral-field dependence should reflect the widely-held belief that the carrier drift velocity saturates for large lateral fields. Two popular expressions which satisfy this

constraint are the Caughey-Thomas and Scharfetter-Gummel dependences.

Two new inversion-layer-specific mobility models have been implemented in the CODECS mixed-level circuit and device simulator. These field-dependent models include both normal and lateral-field mobility degradation. Due to constraints of the device simulator, only the local mobility approach and surface-field-dependent hybrid mobility approach can be chosen to model the normal-field dependence of the mobility. The local mobility approach does not lead to extracted effective mobilities which are uniquely defined by the effective normal field. However, in practical situations, the error introduced may be within acceptable limits. If not, the more accurate, hybrid mobility approach should be used. Several design choices which have an impact on the convergence behavior of the numerical algorithms embedded in the device simulator have been investigated. In particular, it has been determined that calculations which rely on the Jacobian and other derivatives of the semiconductor device equations need to compute these quantities accurately, not just approximations to them. When computing the normal and lateral components of the electric field, a simple test indicates that they can be computed in reference to either the direction of current-flow or the direction of the Si-SiO2 interface. However, the simpler *direction-of-interface* method requires less time to perform the necessary calculations than the *direction-of-current-flow* method.

The normal-field dependencies of the new mobility models have been tested by extracting the effective mobility from simulations of MOSFET's operating in the linear region. The extracted mobility has been compared to curves based on the experimental work of Watt and Plummer. This comparison shows that the mobility calculated using the hybrid-approach model is consistently quite accurate. The local-approach effective mobility is somewhat less accurate. However, the addition of either normal-field dependence significantly improves the accuracy of simulation when comparison is made to the original CODECS mobility model. Even though the hybrid-approach model has performance superior to that of the local-approach model, in some situations the local mobility approach may be preferred for its relative simplicity. If the error introduced by its slightly inaccurate normal-field dependence is not tolerable, it can be reduced by tailoring the mobility model parameters to the

application at hand. Because the drain-to-source current of a MOSFET operating in the linear region is directly proportional to the effective mobility, I_{DS} versus V_{GS} characteristics will be improved when using the new models.

More complete testing of the new models is warranted. Comparison of simulations of the MOSFET drain-current to experimental data should be performed over a wide range of applied biases. In particular, simulation of MOSFET's operating in the saturation region would test the lateral-field dependence and its interaction with the normal-field dependence. Other future work might include the development of a more sophisticated expression for the normal-field dependence. Because of the modular structure of the new mobility model, such an expression could easily be implemented in CODECS.

Appendix A

Equations for Mobility and its Derivatives

This appendix presents the new CODECS expressions for the electron and hole inversion-layer mobilities. It also contains the derivatives of these functions with respect to the normal and lateral components of the electric field.

A.1 Mobility, μ

$$
\begin{aligned}
\mu_{LV} &= \mu_0 \\
\mu_{SR} &= f(\mu_{LV}, E_\perp) \\
\mu_{HC} &= g(\mu_{SR}, E_\parallel) \\
\mu &\equiv \mu_{HC}
\end{aligned}
\tag{A.1}
$$

A.1.1 Normal-Field Dependence

$$
\mu_{SR} = \frac{\mu_{LV}}{1 + \theta_a E_\perp + \theta_b E_\perp{}^2}
\tag{A.2}
$$

A.1.2 Lateral-Field Dependence

$$
\mu_{HC} = \frac{\mu_{SR}}{\left(1 + \left(\frac{\mu_{SR} E_\parallel}{v_{sat}}\right)^\beta\right)^{\frac{1}{\beta}}}
\tag{A.3}
$$

OR

43

$$\mu_{HC} = \frac{\mu_{SR}}{\sqrt{1 + \frac{(\mu_{SR}E_{\parallel}/v_{ac})^2}{(\mu_{SR}E_{\parallel}/v_{ac})+A} + \left(\frac{\mu_{SR}E_{\parallel}}{v_{sat}}\right)^2}} \tag{A.4}$$

A.2   Derivative with respect to Normal Field

$$\frac{\partial \mu_{HC}}{\partial E_{\perp}} = \frac{\partial \mu_{HC}}{\partial \mu_{SR}} \frac{\partial \mu_{SR}}{\partial E_{\perp}} \tag{A.5}$$

$$\frac{\partial \mu_{HC}}{\partial \mu_{SR}} = \frac{1}{\left(1 + \left(\frac{\mu_{SR}E_{\parallel}}{v_{sat}}\right)^{\beta}\right)^{\frac{1}{\beta}+1}} \tag{A.6}$$

OR

$$\frac{\partial \mu_{HC}}{\partial \mu_{SR}} = \frac{1 + \frac{1}{2}\frac{(\mu_{SR}E_{\parallel}/v_{ac})^3}{\left((\mu_{SR}E_{\parallel}/v_{ac})+A\right)^2}}{\left(1 + \frac{(\mu_{SR}E_{\parallel}/v_{ac})^2}{(\mu_{SR}E_{\parallel}/v_{ac})+A} + \left(\frac{\mu_{SR}E_{\parallel}}{v_{sat}}\right)^2\right)^{\frac{3}{2}}} \tag{A.7}$$

$$\frac{\partial \mu_{SR}}{\partial E_{\perp}} = \frac{-\mu_{LV}(\theta_a + 2\theta_b E_{\perp})}{\left(1 + \theta_a E_{\perp} + \theta_b E_{\perp}^2\right)^2} \tag{A.8}$$

A.3   Derivative with respect to Lateral Field

$$\frac{\partial \mu_{HC}}{\partial E_{\parallel}} = \frac{-\mu_{SR}\left(\frac{\mu_{SR}E_{\parallel}}{v_{sat}}\right)^{\beta-1}\frac{\mu_{SR}}{v_{sat}}}{\left(1 + \left(\frac{\mu_{SR}E_{\parallel}}{v_{sat}}\right)^{\beta}\right)^{\frac{1}{\beta}+1}} \tag{A.9}$$

OR

$$\frac{\partial \mu_{HC}}{\partial E_{\parallel}} = \frac{-\frac{1}{2}\mu_{SR}\left[\frac{\left(\frac{\mu_{SR}E_{\parallel}}{v_{ac}}\right)+2A}{\left(\left(\frac{\mu_{SR}E_{\parallel}}{v_{ac}}\right)+A\right)^2}\left(\frac{\mu_{SR}E_{\parallel}}{v_{ac}}\right)\frac{\mu_{SR}}{v_{ac}} + 2\left(\frac{\mu_{SR}E_{\parallel}}{v_{sat}}\right)\frac{\mu_{SR}}{v_{sat}}\right]}{\left(1 + \frac{(\mu_{SR}E_{\parallel}/v_{ac})^2}{(\mu_{SR}E_{\parallel}/v_{ac})+A} + \left(\frac{\mu_{SR}E_{\parallel}}{v_{sat}}\right)^2\right)^{\frac{3}{2}}} \tag{A.10}$$

Appendix B

Supplement to the CODECS User's Guide

B.1   Summary

This appendix is an addition to the original CODECS User's Guide found in [MAYA88]. The input to CODECS includes a description of the parameters of a semiconductor device. Several new features have been added to the numerical MOS-FET (NUMOS) description in order to accommodate the new inversion-layer mobility model. New parameters control where and when the model is to be used. Two others allow the initial field-independent mobilities of electron and holes to be specified by the user. These features are only recognized as part of NUMOS model descriptions; they are invalid for all other model types. In addition to these parameters, a convergence tolerance parameter has been added to allow greater control over termination of the iterative solution process.

B.2   Channel Description

The CHANNEL parameter is used to specify those edges of the simulation mesh where the inversion-layer mobility model should be used instead of the original bulk mobility model. The channel should include the area of the mesh where the inversion layer forms. All edges not included in a channel use the bulk mobility model to compute the mobility.

General form:

CHANNEL INTERFACE XMESHLO XMESHHI YMESHLO YMESHHI

INTERFACE specifies the side of the channel which is the Si-SIO2 interface: it is 0 for the top edge, 1 for the right edge, 2 for the bottom edge, and 3 for the left edge. XMESHLO, XMESHHI, YMESHLO and YMESHHI are mesh indices that

define the bounding rectangle of the channel. All edges on or within this rectangle are part of the channel.

Example:

      CHANNEL 0 9 23 5 25

      The above command specifies a horizontal channel with the interface above it, inside the rectangle with corners at (9,5), (9,25), (23,5), and (23,25).

B.3   Inversion-Layer Mobility Model Parameters

      The following parameters are used to control when to use the inversion-layer mobility model and the values of the field-independent mobilities:

Name	Description	Type	Default
SURFMOB	Use Surface (Inversion-Layer) Mobility Model	Flag	Not Used
MUNS	Field-Independent Electron Surface Mobility	Real	$991\,cm^2/Vs$
MUPS	Field-Independent Hole Surface Mobility	Real	$240\,cm^2/Vs$

B.4   Convergence Tolerance Parameter

      During DC analyses, the iterative solution process terminates when the maximum error in the discretized semiconductor equations falls below a certain absolute tolerance. As the size of the simulation mesh increases, the absolute error in the solution of these equations also increases. More mesh points are needed for MOSFET models that use the inversion-layer mobility model in order to accurately compute the mobility in the inversion layer. During simulation of such devices, it is possible for the maximum solution error to exceed the default tolerance, even though the iteration process has reached a steady state. In such cases it is useful to relax the maximum error tolerance. The following parameter sets the error tolerance for the device equations:

Name	Description	Type	Default
DEVTOL	Maximum Error in Device Equations	Real	1e-8

B.5   MOSFET Example

      The following CODECS input file is used to simulate the I_{DS} versus V_{GS} behavior of an NMOS transistor operating in the linear region. The geometry of the MOSFET is given in Figure B.1. This simulation uses the new inversion-layer mobility model by specifying both the SURFMOB flag and a CHANNEL region.

In addition, the error tolerance, DEVTOL, has been increased to 1e-7 in order to improve convergence behavior.

```
* NMOSFET : IDS VS VGS - LINEAR REGION
VDD 1 0 50mv
VGG 2 0 0.0v
VSS 3 0 0.0v
VBB 4 0 0.0v
N1 1 2 3 4 NMOD width = 10um
***** 2UM N-CHANNEL MOSFET *****
.model NMOD numos
+ concmob fieldmob surfmob
+ xmesh  1 0.0 xmesh  4 0.6 xmesh  5 0.7
+ xmesh  7 1.0 xmesh 11 1.2 xmesh 21 3.2 xmesh 25 3.4
+ xmesh 27 3.7 xmesh 28 3.8 xmesh 31 4.4
+ ymesh  1 -.0875  ymesh  5 0.0
+ ymesh  6 1.00e-4 ymesh  7 1.75e-4 ymesh  8 3.06e-4
+ ymesh  9 5.36e-4 ymesh 10 9.38e-4 ymesh 11 1.64e-3
+ ymesh 12 2.87e-3 ymesh 13 5.03e-3 ymesh 14 8.81e-3
+ ymesh 15 1.54e-2 ymesh 16 2.70e-2
+ ymesh 25 0.30 ymesh 30 2.0
+ unif 1e19 0 1.1 0 0.2
+ unif 1e19 3.3 4.4 0 0.2
+ unif -2.5e16 0 4.4 0 2.0
+ oxide 5 27 1 5
+ silicon 1 31 5 30
+ channel 0 9 23 5 25
+ contact 28 31 5 5
+ contact 5 27 1 1
+ contact 1 4 5 5
+ contact 1 31 30 30
+ devtol 1e-7
.OPTION ACCT BYPASS=0
.DC VGG 0.0v 5.0v 0.1v
.PLOT DC I(VSS)
.END
```

Appendix C

The DSIM Device Simulator

C.1 Summary

Calculation of the mobility is only one part of the MOS device simulation problem changed by the new field-dependent inversion-layer mobility model. Implementation of a the new model entails a number of modifications to the data structures and algorithms of the DSIM device simulator. This appendix reviews the structure and physical basis of the original DSIM implementation. Throughout the presentation, material related to the mobility is emphasized. Changes due to the new inversion-layer mobility model are presented in Chapter 4. For simplicity, attention is restricted to the algorithms for calculating DC operating points and DC transfer curves. A more thorough discussion of DSIM can be found in [MAYA88].

The basic partial-differential equations governing semiconductor device operation are introduced in normalized form. Restriction to DC steady-state analyses allows time-dependent terms to be dropped from the equations. Finite difference discretization in space is applied. The data structures representing the discretized device are described.

Next, the algorithm and data structures used to calculate a DC operating point are presented. DC transfer curve analysis is considered as a sequence of related DC operating point analyses. The projection algorithm used to calculate the initial guess at one bias point from the solution at the previous bias point is outlined.

C.2 The Fundamental Semiconductor Equations

DSIM is based upon the solution of Poisson's equation and the electron and hole current-continuity equations. These are expressed in normalized form as:

$$\nabla \cdot \mathbf{E} = (N_D - N_A + p - n) \tag{C.1}$$

$$\nabla \cdot \mathbf{J}_n = \frac{\partial n}{\partial t} - U_{GR} \tag{C.2}$$

$$\nabla \cdot \mathbf{J}_p = -\frac{\partial p}{\partial t} + U_{GR} \qquad (C.3)$$

where

$$\mathbf{E} = -\nabla \Psi \qquad (C.4)$$

$$\mathbf{J}_n = -\mu_n (n\nabla \Psi - \nabla n) \qquad (C.5)$$

$$\mathbf{J}_p = -\mu_p (p\nabla \Psi + \nabla p) \qquad (C.6)$$

and

Ψ	=	electrostatic potential
n (p)	=	electron (hole) concentration
$\mathbf{E}$	=	electric field
$\mathbf{J}_n$ $(\mathbf{J}_p)$	=	electron (hole) current density
μ_n (μ_p)	=	electron (hole) mobility
N_D (N_A)	=	donor (acceptor) concentration
U_{GR}	=	net generation-recombination rate

The above equations are solved for the unknown distributions of the electrostatic potential and carrier concentrations, Ψ, n, and p, in the silicon regions of a device. In the oxide regions of a device, Laplace's equation, $\Delta^2 \Psi = 0$, is solved for the potential Ψ alone. Voltage biases applied to the terminals of a device are used to calculate boundary conditions for the semiconductor equations. Several boundary conditions are used, each applicable to a different type of contact between the voltage terminal and the device. Boundary conditions are reviewed in Chapter 3 of [MAYA88]. Parameters in the equations such as mobilities and dopant concentrations are determined by appropriate physical modelling.

The current densities, $\mathbf{J}_n$ and $\mathbf{J}_p$, can also be expressed in terms of the quasi-fermi potential gradients, $\mathbf{F}_n$ and $\mathbf{F}_p$:

$$\mathbf{J}_n = -\mu_n n \mathbf{F}_n \qquad (C.7)$$

$$\mathbf{J}_p = -\mu_p p \mathbf{F}_p \qquad (C.8)$$

where

$$\mathbf{F}_n = \nabla \Psi - \frac{1}{n} \nabla n \qquad (C.9)$$

$$\mathbf{F}_p = \nabla \Psi + \frac{1}{p} \nabla p \qquad (C.10)$$

C.3 Two-Dimensional Discretization

The set of basic semiconductor equations must be converted to a form suitable for implementation in a numerical device simulator. The continuous domain of

a semiconductor device is approximated by a discrete rectangular simulation mesh. Figure C.1 shows a portion of such a mesh near the Si-SiO2 interface of an MOS device.

The semiconductor equations are approximated on the simulation mesh using the method of finite differences. A complete derivation of the discretized equations is beyond the scope of this appendix, but can be found in Chapter 5 of [MAYA88]. For DC steady-state analyses, the time derivatives, $\frac{\partial n}{\partial t}$ and $\frac{\partial p}{\partial t}$, can be dropped from the current-continuity equations. The resulting time-independent discretized equations at node (i, j) of the mesh, marked A in Figure C.1, are given below:

$$-E_y|_{i,j-\frac{1}{2}}\Delta x_i + E_x|_{i+\frac{1}{2},j}\Delta y_j + E_y|_{i,j+\frac{1}{2}}\Delta x_i - E_x|_{i-\frac{1}{2},j}\Delta y_j$$
$$= (N_D - N_A + p - n)|_{i,j}\Delta x_i\Delta y_j \qquad (C.11)$$

$$-J_{ny}|_{i,j-\frac{1}{2}}\Delta x_i + J_{nx}|_{i+\frac{1}{2},j}\Delta y_j + J_{ny}|_{i,j+\frac{1}{2}}\Delta x_i - J_{nx}|_{i-\frac{1}{2},j}\Delta y_j$$
$$= -(U_{GR})|_{i,j}\Delta x_i\Delta y_j \qquad (C.12)$$

$$-J_{py}|_{i,j-\frac{1}{2}}\Delta x_i + J_{px}|_{i+\frac{1}{2},j}\Delta y_j + J_{py}|_{i,j+\frac{1}{2}}\Delta x_i - J_{px}|_{i-\frac{1}{2},j}\Delta y_j$$
$$= (U_{GR})|_{i,j}\Delta x_i\Delta y_j \qquad (C.13)$$

where

$$\Delta x_i = \frac{\Delta x_{i+\frac{1}{2}} + \Delta x_{i-\frac{1}{2}}}{2} \qquad (C.14)$$

$$\Delta y_j = \frac{\Delta y_{j+\frac{1}{2}} + \Delta y_{j-\frac{1}{2}}}{2} \qquad (C.15)$$

The components of $\mathbf{E}$, $\mathbf{J}_n$, and $\mathbf{J}_p$ are estimated in terms of the unknowns Ψ, n, and p. The electric field is calculated from a simple divided difference, and a quasi-2D Scharfetter-Gummel discretization scheme is used for the current densities. For the edge $(i + \frac{1}{2}, j)$, marked B in Figure C.1, the formulas are:

$$E_x|_{i+\frac{1}{2},j} = -\frac{\Delta\Psi_{i+\frac{1}{2},j}}{\Delta x_{i+\frac{1}{2}}} \qquad (C.16)$$

$$J_{nx}|_{i+\frac{1}{2},j} = \mu_n|_{i+\frac{1}{2},j}\frac{\left[n_{i+1,j}B(\Delta\Psi_{i+\frac{1}{2},j}) - n_{i,j}B(-\Delta\Psi_{i+\frac{1}{2},j})\right]}{\Delta x_{i+\frac{1}{2}}} \qquad (C.17)$$

$$J_{px}|_{i+\frac{1}{2},j} = \mu_p|_{i+\frac{1}{2},j}\frac{\left[p_{i,j}B(\Delta\Psi_{i+\frac{1}{2},j}) - p_{i+1,j}B(-\Delta\Psi_{i+\frac{1}{2},j})\right]}{\Delta x_{i+\frac{1}{2}}} \qquad (C.18)$$

where $B(x) = \frac{x}{e^x-1}$ is the Bernoulli function, and $\Delta\Psi_{i+\frac{1}{2},j} = \Psi_{i+1,j} - \Psi_{i,j}$. The mobilities, $\mu_n|_{i+\frac{1}{2},j}$ and $\mu_p|_{i+\frac{1}{2},j}$, are calculated using the original DSIM mobility model.

C.4 Device Data Structure

Figure C.2 shows a graphic representation of the key data structures used to represent a device. Three types of objects are shown: elements, nodes and edges. Elements store dimensional information (Δx and Δy) and the local material type (SILICON or OXIDE). Nodes store the solution variables, (Ψ, n, p), and other quantities subscripted (i,j) in the discretized equations. Edges store quantities that are evaluated midway between adjacent nodes, such as the mobility, μ, and current density, J. Pointers in the data structures interlink them according to their relative positions. This allows efficient and easy access to all quantities in the vicinity of a particular node or edge. The new inversion-layer mobility model takes advantage of this feature of the data structure.

C.5 DC Operating Point Analysis

Finite difference discretization of the semiconductor equations creates a system of coupled nonlinear algebraic equations. This system can be expressed in the form:

$$F(u) = 0 \qquad (C.19)$$

where u is the vector of unknown potentials and electron and hole concentrations, $\Psi_{i,j}$, $n_{i,j}$ and $p_{i,j}$. An iterative norm-reducing Newton method is used to find the vector of unknowns, u^*, which satisfies these equations. An initial guess, u^0, is made by solving Poisson's equation at thermal equilibrium where no currents flow. The initial guess is incrementally updated at each iteration until the solution is reached. The kth Newton update, Δu^k, solves the matrix equation:

$$J(u^k)\Delta u^k = -F(u^k) \qquad (C.20)$$

where $J(u^k)$ is the Jacobian of the equations, evaluated as a function of the present solution guess. The next solution guess, u^{k+1}, is then computed using the formula:

$$u^{k+1} = u^k + \lambda^k \Delta u^k \qquad (C.21)$$

where λ^k is a varying parameter, less than or usually equal to one. Thus, at each iteration, the values of the functions, $F(u^k)$, and their Jacobian, $J(u^k)$, are computed. The new DSIM inversion-layer mobility model changes both of these computations.

Computation of the Jacobian matrix and right-hand side (RHS) in Equation C.20 is divided into two major parts in DSIM. In the first step, several physical quantities are precalculated and stored in the node and edge data structures. Then, these precomputed values are used to load the Jacobian and RHS data structures. Many of the values are used to calculate multiple entries in these structures. By saving and reusing them, computational time is reduced.

C.6 DC Transfer Curve Analysis

A DC transfer curve consists of a sequence of DC operating point analyses where one of the applied biases is varied between operating points. The initial guess at bias point $m + 1$, $\mathbf{u}^0_{m+1}$, can be calculated from the solution at bias point m, $\mathbf{u}^\star_m$, using a forward-Euler scheme:

$$\mathbf{u}^0_{m+1} = \mathbf{u}^\star_m + \left(\frac{\partial \mathbf{u}}{\partial V}\right)^\star_m \Delta V \tag{C.22}$$

where ΔV is the voltage change between bias point $m + 1$ and m. If the dependence on the varying bias voltage, V, is made explicit in Equation C.19, it becomes:

$$\mathbf{F}(\mathbf{u}(V), V) = 0 \tag{C.23}$$

Differentation of the above equation with respect to V and rearrangement of the result give the following matrix equation for $\left(\frac{\partial \mathbf{u}}{\partial V}\right)^\star_m$:

$$\mathbf{J}(\mathbf{u}^\star_m)\left(\frac{\partial \mathbf{u}}{\partial V}\right)^\star_m = \frac{\partial \mathbf{F}}{\partial V} \tag{C.24}$$

This equation can be solved and the resulting $\left(\frac{\partial \mathbf{u}}{\partial V}\right)^\star_m$ can be substituted in Equation C.22 to obtain $\mathbf{u}^0_{m+1}$. The actual implementation of this approach in DSIM involves some minor adjustments to the above algorithm. However, formation of the vector $\frac{\partial \mathbf{F}}{\partial V}$ is still required. The new inversion-layer mobility model changes this calculation.

Appendix D

Hybrid Mobility Expressions

In this appendix, the two hybrid mobility expressions mentioned in Section 4.3 are derived. One of these expressions depends on the local and bulk normal fields, while the other depends on the local and surface normal fields. The derivations closely follow the arguments in [SHIN89], but a modification of their approach is made in order to obtain the new surface-field-dependent expression.

The starting point for both derivations is the same: the expected effective mobility equation, Equation 3.2. For convenience, this expression for μ_{eff}^{exp} is repeated here [SHIN89, eq. (7b)]:

$$\mu_{eff}^{exp} = \frac{\int_{E_{\perp}^{bulk}}^{E_{\perp}^{surf}} \mu_{local}(E_{\perp}) dE_{\perp}}{E_{\perp}^{surf} - E_{\perp}^{bulk}} \tag{D.1}$$

where $E_{\perp}^{surf}$ and $E_{\perp}^{bulk}$ are the surface and bulk normal fields at the edges of a cross-section of the channel. The expected effective mobility should match a desired effective mobility curve, μ_{eff}^{des}, when both are plotted versus the effective normal field:

$$E_{\perp}^{eff} = \alpha E_{\perp}^{bulk} + \beta E_{\perp}^{surf} \tag{D.2}$$

where the parameters α, β have been determined empirically to be $\frac{1}{2}, \frac{1}{2}$ for electrons and $\frac{2}{3}, \frac{1}{3}$ for holes. The two effective mobilities coincide when the following relation is satisfied:

$$\mu_{eff}^{des}(E_{\perp}^{eff}) = \frac{\int_{E_{\perp}^{bulk}}^{E_{\perp}^{surf}} \mu_{local}(E_{\perp}) dE_{\perp}}{E_{\perp}^{surf} - E_{\perp}^{bulk}} \tag{D.3}$$

Although the dependence of μ_{eff}^{des} on $E_{\perp}^{eff}$ is the only one explicitly recognized in the above equation, other dependences can be included. However, one condition on these dependences is that they cannot involve quantities which vary as a function of position in the inversion layer. The other is that they cannot depend on average properties of the inversion layer that are functions of the unknowns: Ψ, n, and p

For example, the average substrate doping near the Si-SiO2 interface would be an acceptable quantity, while either the inversion layer charge concentration, qn, or total inversion layer charge, qN_{inv}, would not.

A bulk-field-dependent hybrid mobility expression for μ_{local} which satisfies Equation D.3 is now obtained. The above equation can be rearranged by multiplying both sides by $\left(E_\perp^{surf} - E_\perp^{bulk} \right)$. This form is differentiated with respect to the surface normal field, $E_\perp^{surf}$ to get an expression for the value of μ_{local} at the surface [SHIN89, eq. (8)]:

$$\mu_{local}(\ E_\perp^{surf}\ ) = \mu_{eff}^{des}(\ E_\perp^{eff}\ ) + \left(E_\perp^{surf} - E_\perp^{bulk} \right) \frac{d\mu_{eff}^{des}}{dE_\perp^{surf}} \qquad (D.4)$$

Finally, the mobility at a point below the surface can be obtained simply by replacing all occurrences of $E_\perp^{surf}$ with the local normal field, $E_\perp^{local}$ [SHIN89, eq. (9)]:

$$\mu_{local}(\ E_\perp^{local},\ E_\perp^{bulk}\ ) = \mu_{eff}^{des}(\ \alpha E_\perp^{bulk} + \beta E_\perp^{local}\ ) + \left(E_\perp^{local} - E_\perp^{bulk} \right) \frac{d\mu_{eff}^{des}}{dE_\perp^{local}} \qquad (D.5)$$

where the dependence of this hybrid mobility expression on $E_\perp^{bulk}$ has been explicitly included. It can be easily verified that the above equation does indeed satisfy Equation D.3.

A surface-field-dependent hybrid mobility expression results from a slight modification of the above argument. If, instead of differentiating Equation D.3 with respect to $E_\perp^{surf}$, the derivative is taken with respect to $E_\perp^{surf}$, then the value of μ_{local} at the bulk edge of the inversion layer is obtained as:

$$\mu_{local}(\ E_\perp^{bulk}\ ) = \mu_{eff}^{des}(\ E_\perp^{eff}\ ) - \left(E_\perp^{surf} - E_\perp^{bulk} \right) \frac{d\mu_{eff}^{des}}{dE_\perp^{bulk}} \qquad (D.6)$$

Once again, $E_\perp^{local}$ is substituted, this time for all occurrences of $E_\perp^{bulk}$. The surface-field-dependent expression obtained is:

$$\mu_{local}(\ E_\perp^{local},\ E_\perp^{surf}\ ) = \mu_{eff}^{des}(\ \alpha E_\perp^{local} + \beta E_\perp^{surf}\ ) - \left(E_\perp^{surf} - E_\perp^{local} \right) \frac{d\mu_{eff}^{des}}{dE_\perp^{local}} \qquad (D.7)$$

This new hybrid mobility expression also satisfies Equation D.3.

References

[CAUG67] Caughey, D. M. and R. E. Thomas, "Carrier Mobilities in Silicon Empirically Related to Doping and Field," *Proc. IEEE,* vol. 52, p. 2192, December 1967.

[FRAN83] Franz, A. F., G. A. Franz, S. Selberherr, and P. Markowich, "The Influence of Various Mobility Models on the Iteration Process and Solution of the Basic Semiconductor Equations," Proc. NASECODE III, Dublin, Ireland, p. 117, June 1983.

[HIRO87] Hiroki, A., S. Odanaka, K. Ohe, and H. Esaki, "A Mobility Model for Submicrometer MOSFET Device Simulations," *IEEE Electron Device Letters,* vol. EDL-8, p. 231, May 1987.

[LEE89] Lee, S.-W., "Universality of Mobility-Gate Field Characteristics of Electrons in the Inversion Charge Layer and Its Application in MOSFET Modeling," *IEEE Trans. Computer-Aided Design,* vol. CAD-8, p. 724, July 1989.

[LIAN86] Liang, M.-S., J. Y. Choi, P.-K. Ko and C. Hu, "Inversion-Layer Capacitance and Mobility of Very Thin Gate-Oxide MOSFET's," *IEEE Trans. Electron Devices,* vol. ED-33, p. 409, March 1986.

[MAYA88] Mayaram, K., *CODECS: A Mixed-Level Circuit and Device Simulator,* UC Berkeley Electronics Research Laboratory, Memorandum No. UCB/ERL M88/71, 1988.

[MULL86] Muller, R. S. and T. I. Kamins, *Device Electronics for Integrated Circuits,* John Wiley and Sons, New York, 1986.

[NISH87] Nishida, T. and C.-T. Sah, "A Physically Based Mobility Model for MOSFET Numerical Simulation," *IEEE Trans. Electron Devices,* vol. ED-34, p. 310, February 1987.

[PADM89] Padmanabhan, S. and A. Rothwarf, "Quantum Inversion Layer Mobility: Numerical Results," *IEEE Trans. Electron Devices,* vol. ED-36, p. 2557, November 1989.

[SABN79] Sabnis, A. G. and J. T. Clemens, "Characterization of the Electron Mobility in the Inverted ¡100¿ Si Surface," IEDM Tech. Dig., p. 18, 1979.

[SCHA69] Scharfetter, D. L. and H. K. Gummel, "Large-Signal Analysis of a Silicon Read Diode Oscillator," *IEEE Trans. Electron Devices,* vol. ED-16, p. 64, January 1969.

[SCHW83] Schwarz, S. A. and S. E. Russek, "Semi-Empirical Equations for Electron Velocity in Silicon: Part II–MOS Inversion Layer," *IEEE Trans. Electron Devices,* vol. ED-30, p. 1634, December 1983.

[SELB85] Selberherr, S., *Analysis and Simulation of Semiconductor Devices,* Springer-Verlag, New York, 1985.

[SHIN89] Shin, H., A. F. Tasch, Jr., C. M. Maziar and S. K. Banerjee, "A New Approach to Verify and Derive a Transverse-Field-Dependent Mobility Model for Electrons in MOS Inversion Layers," *IEEE Trans. Electron Devices,* vol. ED-36, p. 1117, June 1989.

[SUN80] Sun, S. C. and J. D. Plummer, "Electron Mobility in Inversion and Accumulation Layers on Thermally Oxidized Silicon Surfaces," *IEEE Trans. Electron Devices,* vol. ED-27, p. 1497, August 1980.

[THOR80] Thornber, K. K., "Relation of Drift Velocity to Low-Field Mobility and High-Field Saturation Velocity," *J. Appl. Phys.,* vol. 51, p. 2127, April 1980.

[WATT87] Watt, J. T. and J. D. Plummer, "Universal Mobility-Field Curves for Electrons and Holes in MOS Inversion Layers," *Digest of Tech. Papers 1987 Symp. VLSI Technology,* p. 81, May 1987.

[YAMA79] Yamaguchi, K., "Field-Dependent Mobility Model for Two-Dimensional Numerical Analysis of MOSFET's," *IEEE Trans. Electron Devices,* vol. ED-26, p. 1068, July 1979.

[YAMA83] Yamaguchi, K., "A Mobility Model for Carriers in the MOS Inversion Layer," *IEEE Trans. Electron Devices,* vol. ED-30, p. 658, June 1983.

List of Figures

Fig. 2.1: Inversion-Layer Scattering Mechanisms

Fig. 2.2: The Si-SiO2 Interface

a. Idealized Si-SiO2 Interface

b. Real Si-SiO2 Interface

Fig. 2.3: Electron Inversion-Layer Mobility
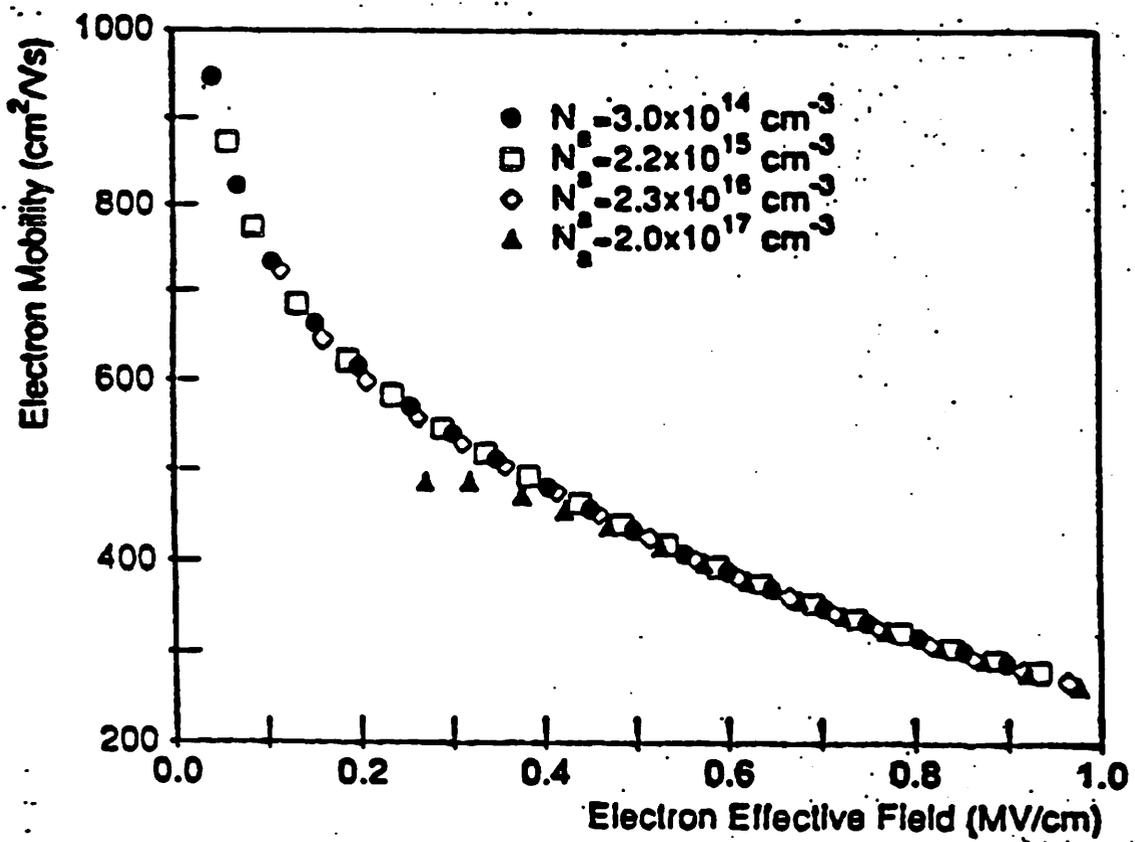
Electron mobility versus effective field for various surface doping densities. [WATT87]

Fig. 2.4: Electron Drift Velocity

Vdrift (10^6 cm/s)

Lateral Electric Field (10^3 V/cm)
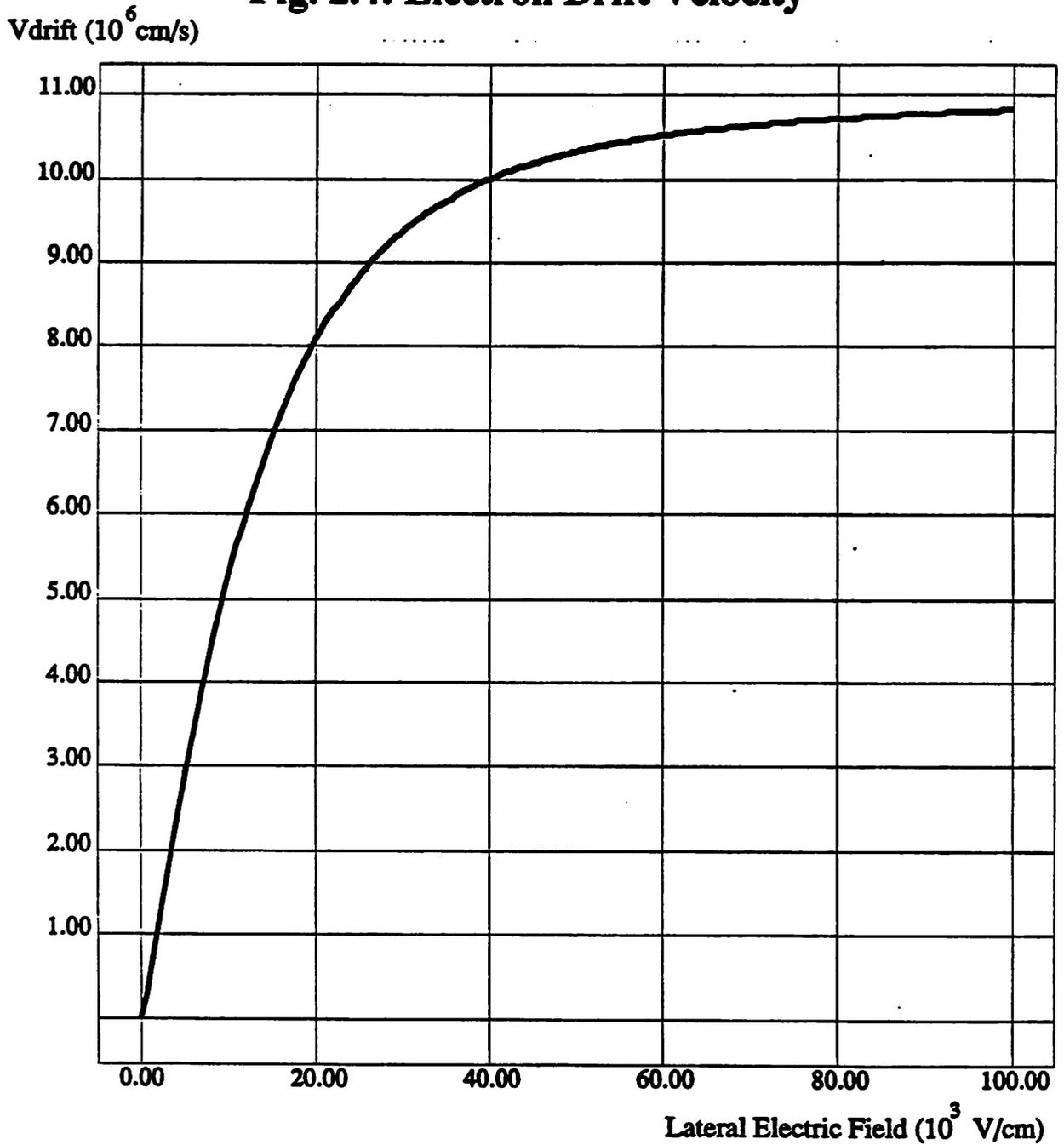
Drift velocity obtained by multiplying Caughey-Thomas lateral-field-dependent electron mobility expression [CAUG67] by lateral-field strength.

$$\mu_0 = 600 \ cm^2/Vs \qquad v_{sat} = 1.1 \times 10^7 \ cm/s$$

Fig. 3.1: Expected Effective Mobility

μ_{eff}^{exp} (cm^2/Vs)

Legend:
- $E_\perp$bulk = 0.0 MV/cm
- $E_\perp$bulk = 0.1 MV/cm
- $E_\perp$bulk = 0.2 MV/cm
- $E_\perp$bulk = 0.3 MV/cm
- $E_\perp$bulk = 0.4 MV/cm
- $E_\perp$bulk = 0.5 MV/cm

$E_\perp^{eff}$ (MV/cm)
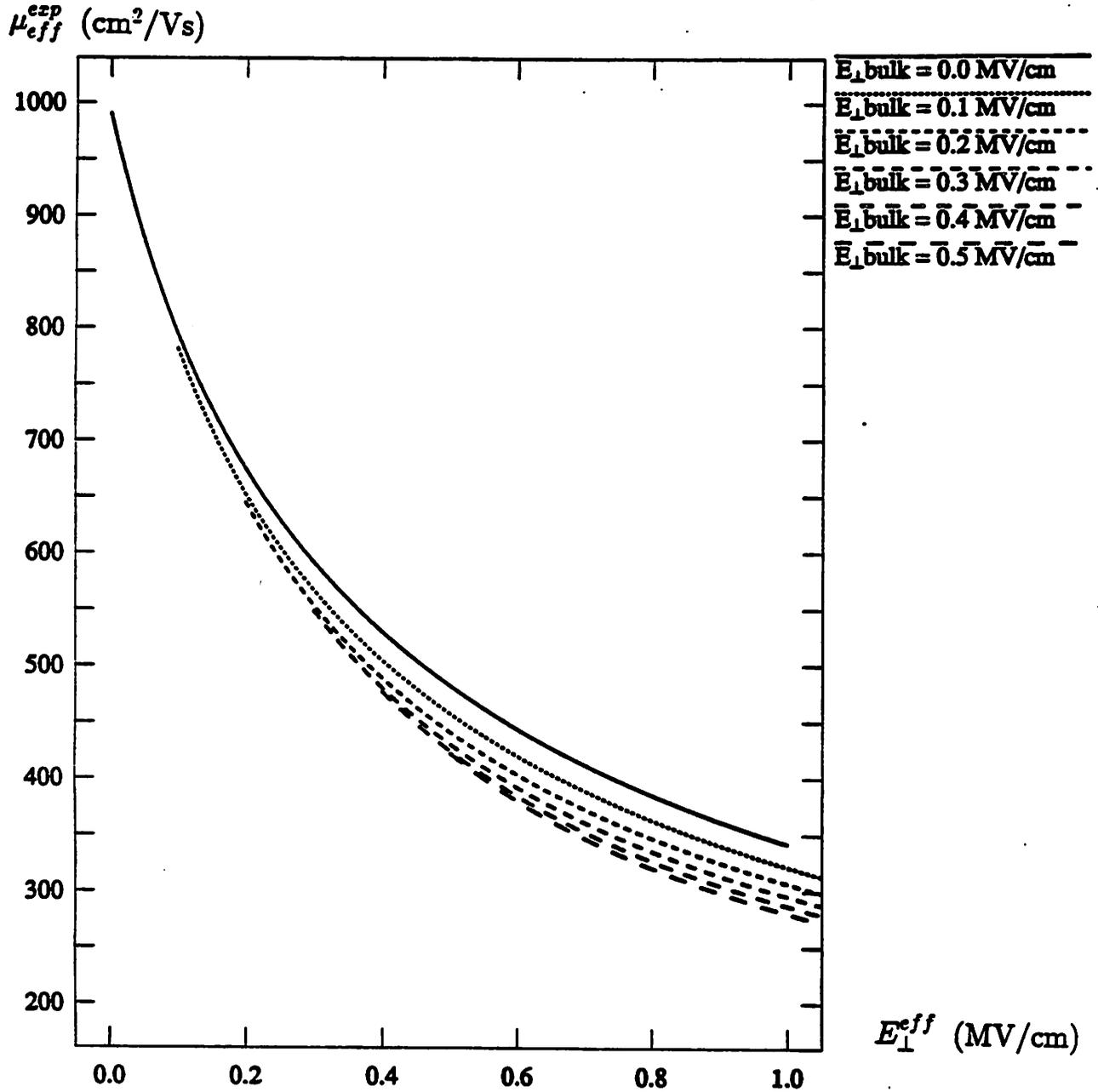
Expected effective mobility versus

effective normal field, $E_\perp^{eff} = \left(\frac{E_\perp^{surf} + E_\perp^{bulk}}{2} \right)$.

Fig. 4.1: Simulation Mesh for MOSFET
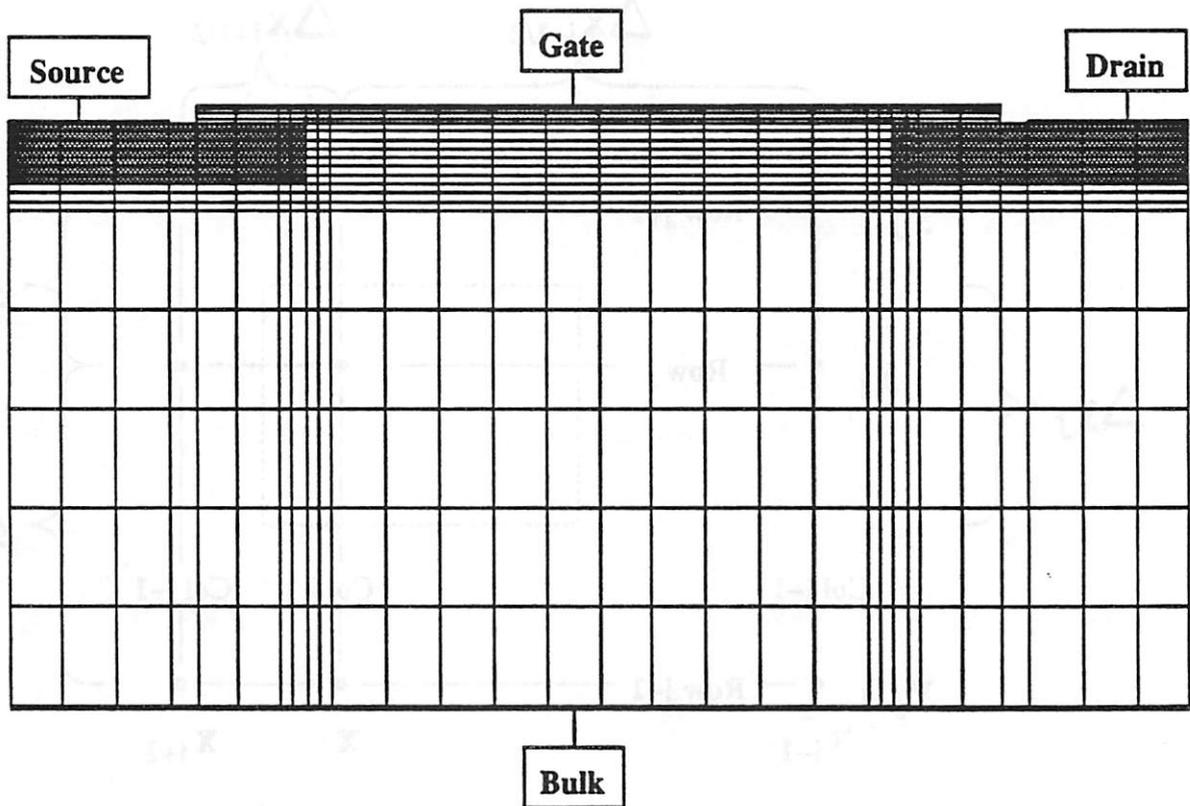
Fig. 4.2: Simulation–Mesh Dimensions
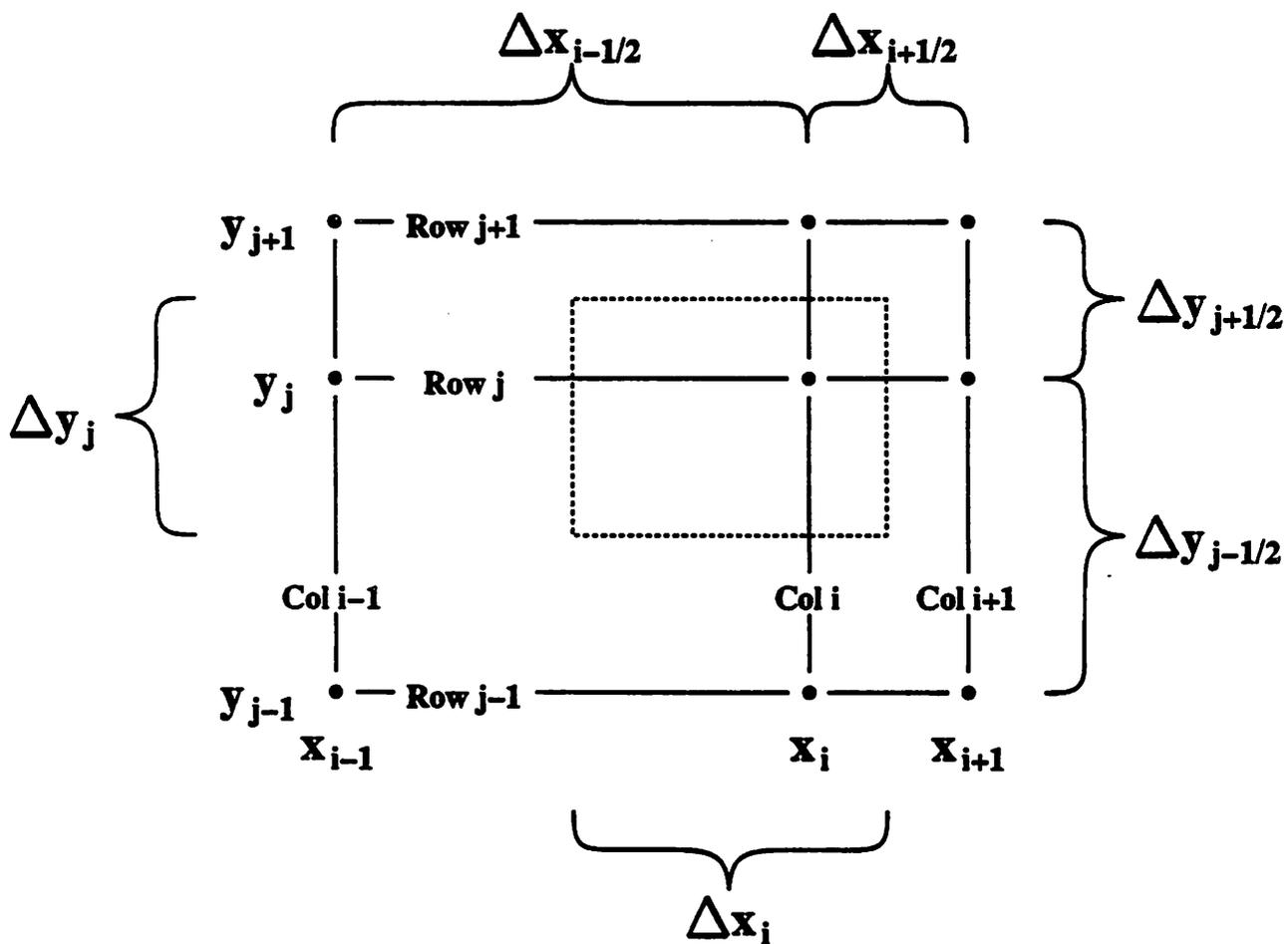
Fig. 4.3: Approaches to Normal–Field Dependence
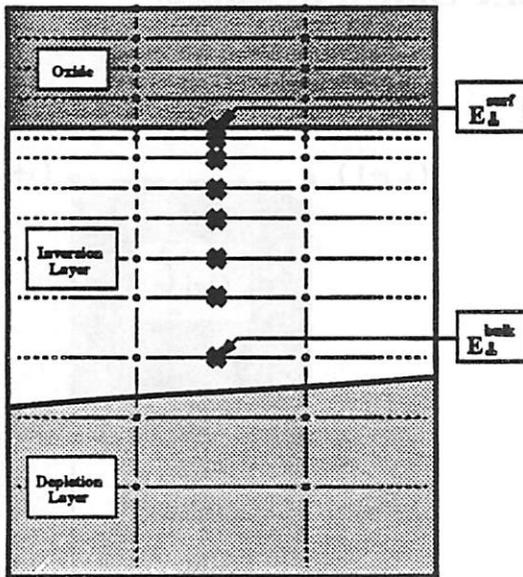
a. Effective Mobility Approach
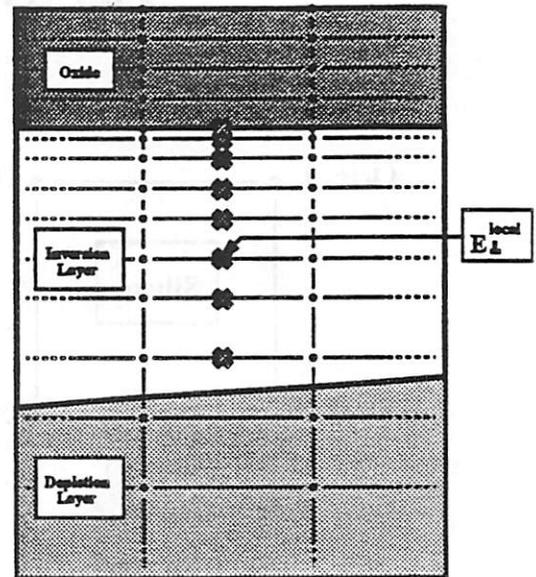
b. Local Mobility Approach
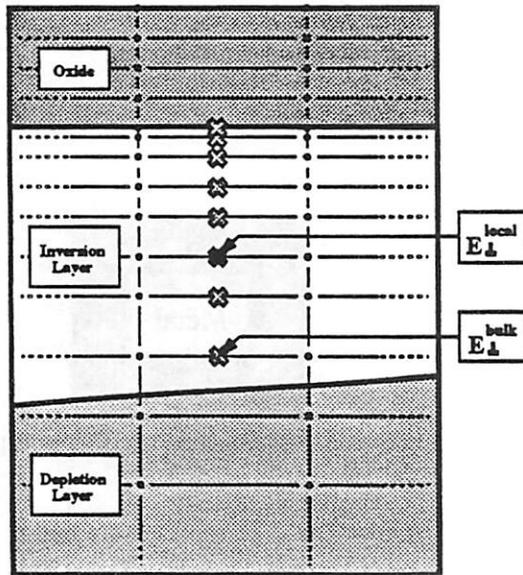
c. Hybrid Mobility Approach
(Local + Bulk Fields)
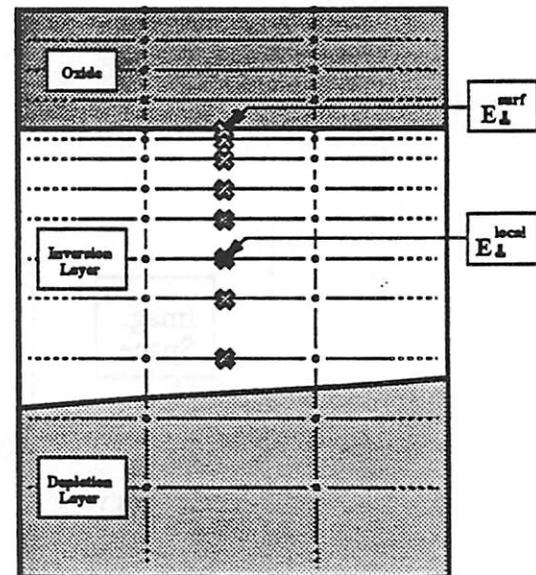
d. Hybrid Mobility Approach
(Local + Surface Fields)

In each figure, the indicated normal fields are used to compute the mobility for edges marked by a dark ✖. For the other edges, marked by a light ✖, the local normal field must be recomputed at each edge.

Fig. 4.4: Element Configurations
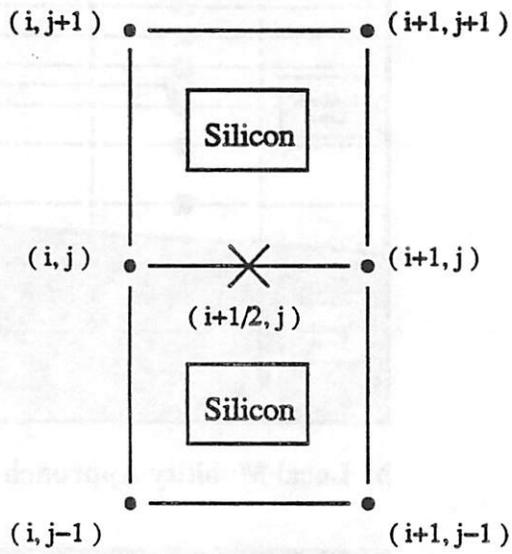
A.
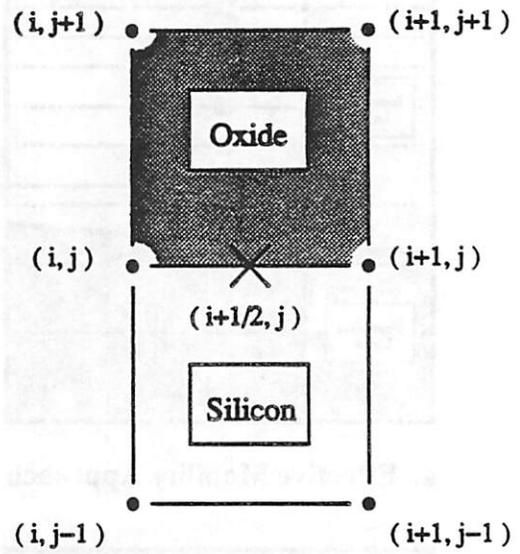
B.
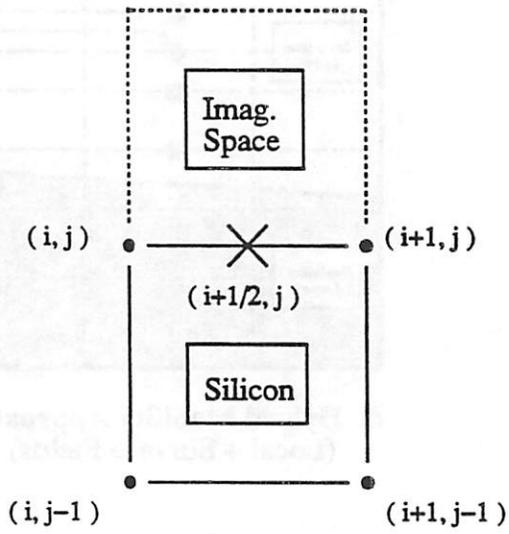
C.
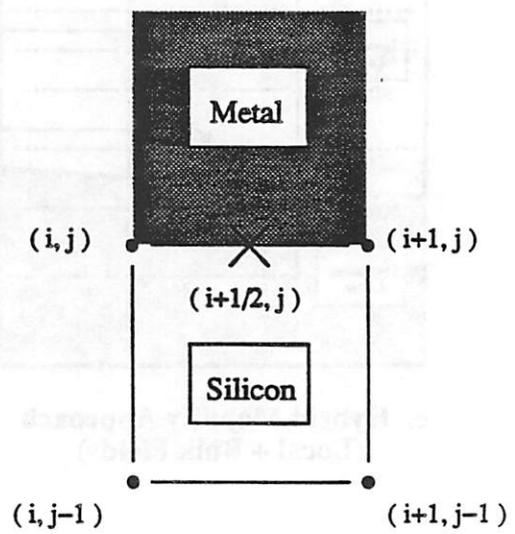
D.

Fig. 4.5: Geometry of Test MOS Transistor

3.0 μm

0.7 μm

0.6 μm

0.4 μm

500 Å

n+ : 1e19

n+ : 1e19

0.2 μm

1.1 μm

2.0 μm

p substrate : 2.5e16
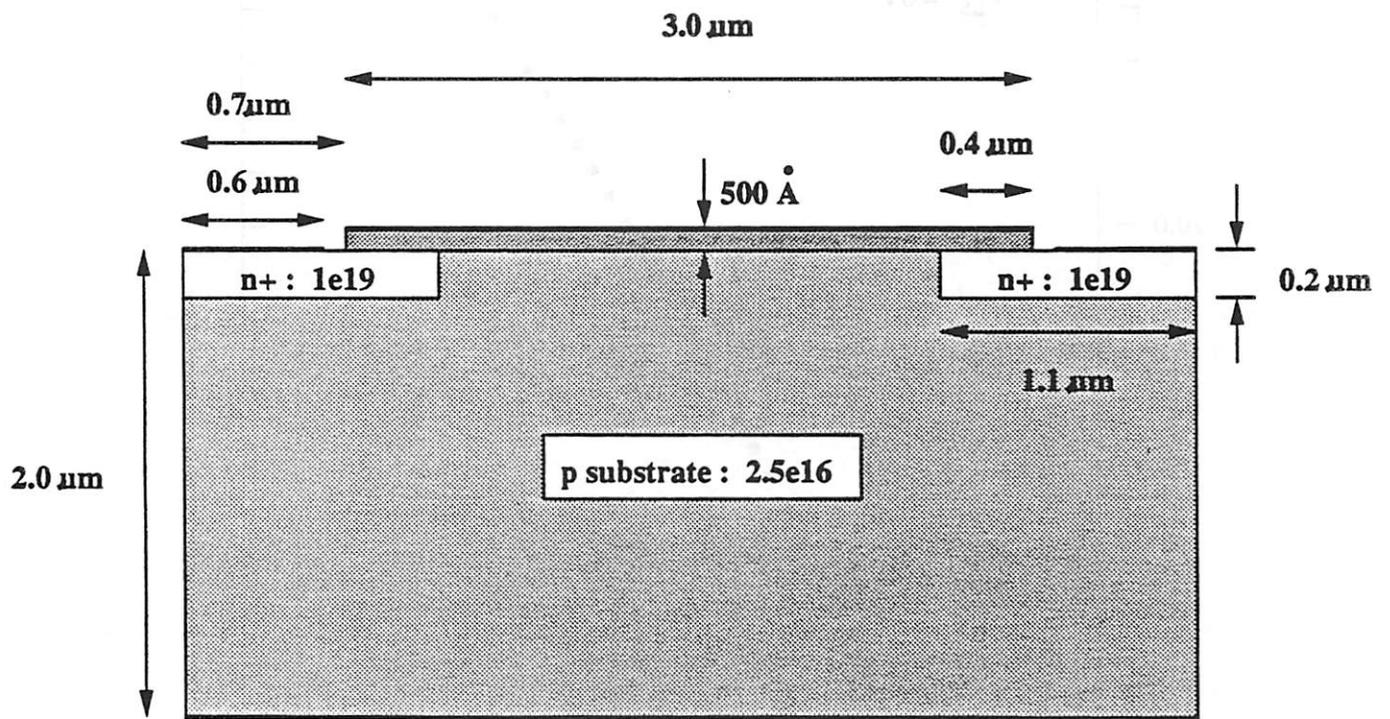
Fig. 4.6a: Linear-Region Drain-Current

I_{DS} (pA)

40.0 —

30.0 — $V_{DS} = 50mV$
                $V_{BS} = 0V$

20.0 —

10.0 —

0.0 —

V_{GS} (V)

0.0   1.0   2.0   3.0   4.0   5.0

□ Interface Ref.
× Current-Flow Ref.
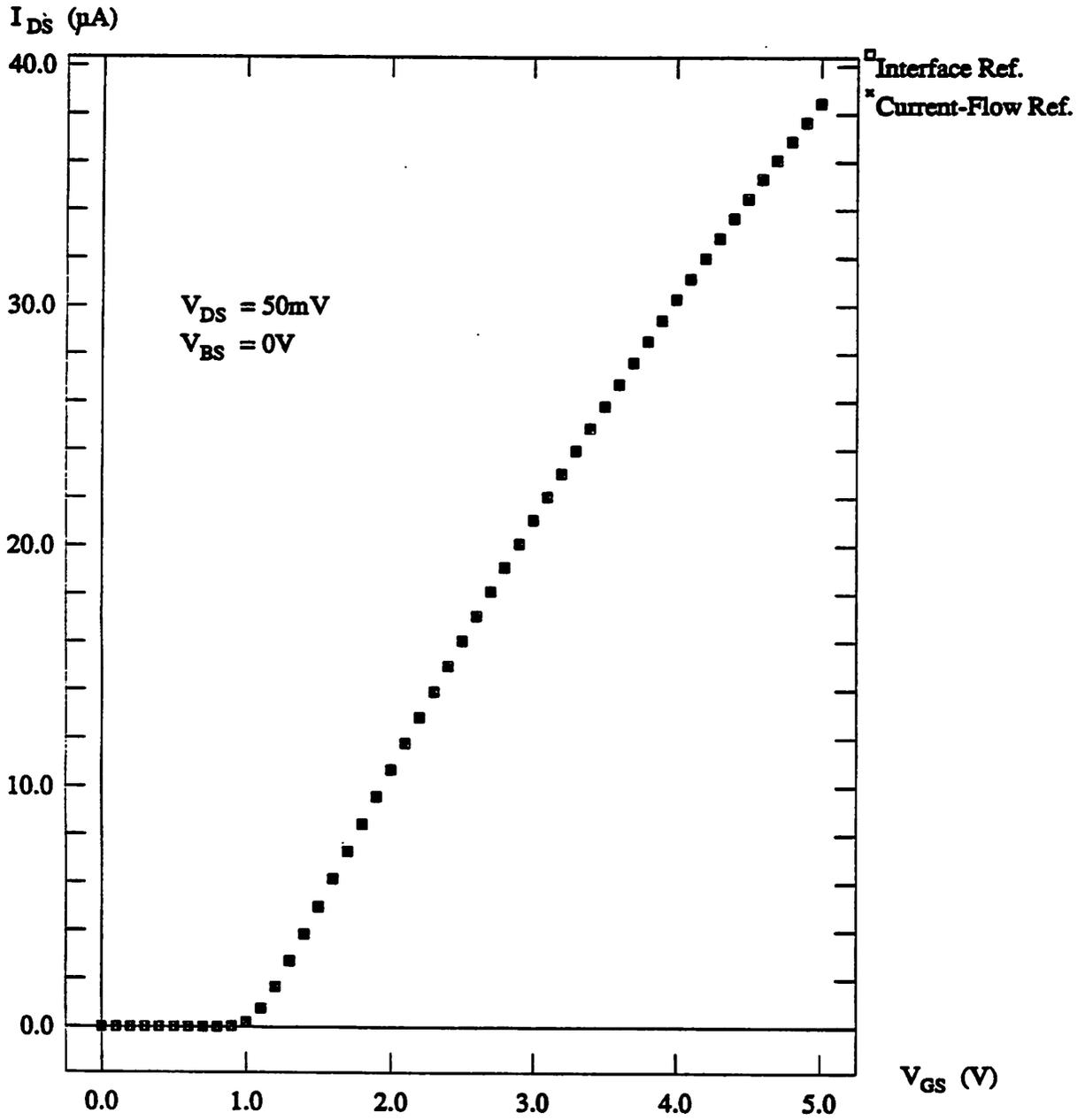
Fig. 4.6b: Saturation-Region Drain-Current

I_{DS} (μA)

□ Interface Ref.
× Current-Flow Ref.

900.0

800.0

700.0

$V_{DS} = 5V$
$V_{BS} = 0V$

600.0

500.0

400.0

300.0

200.0

100.0

0.0

0.0   1.0   2.0   3.0   4.0   5.0

V_{GS} (V)
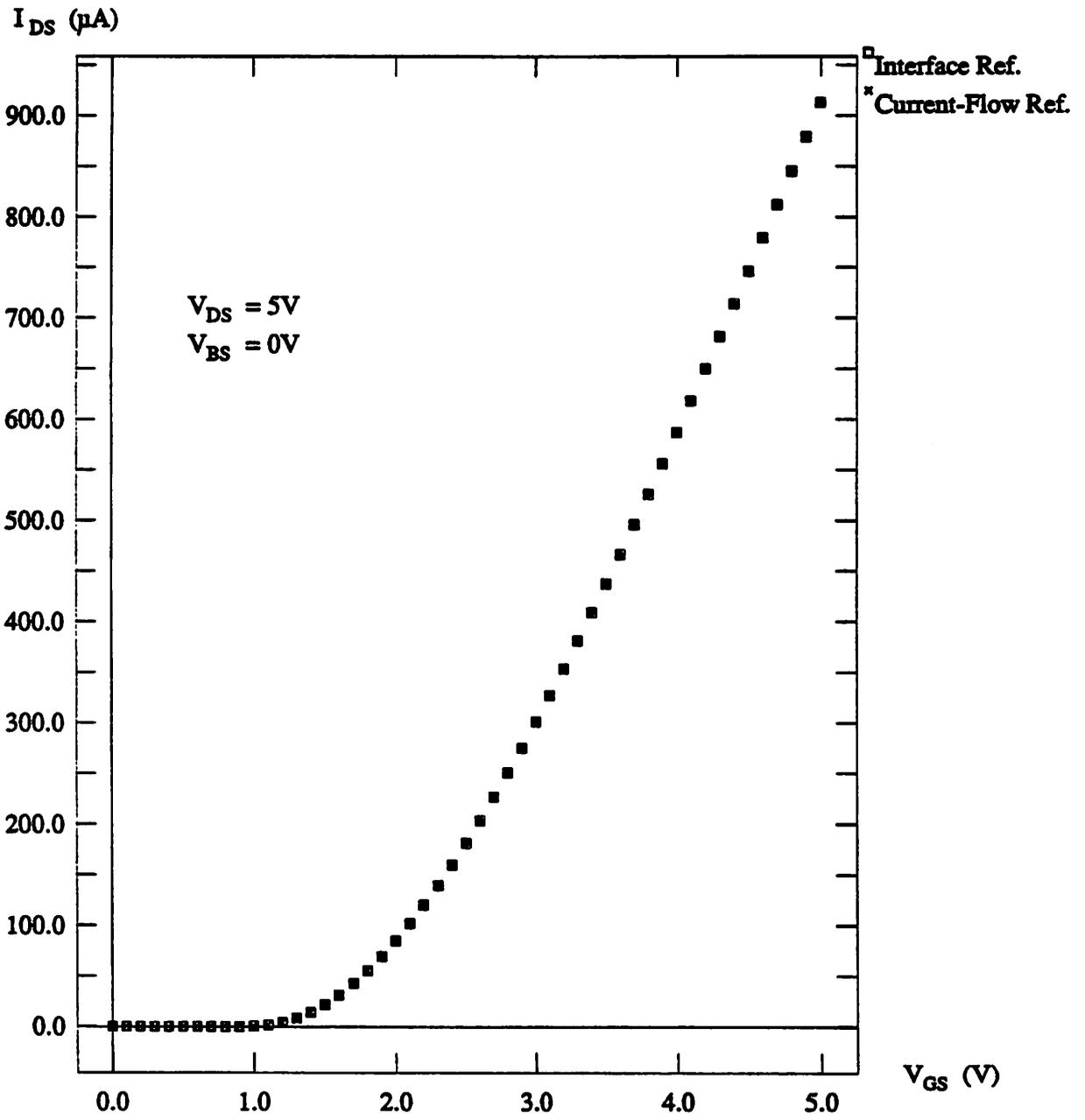
Fig. 5.1: Long Channel NMOS Device
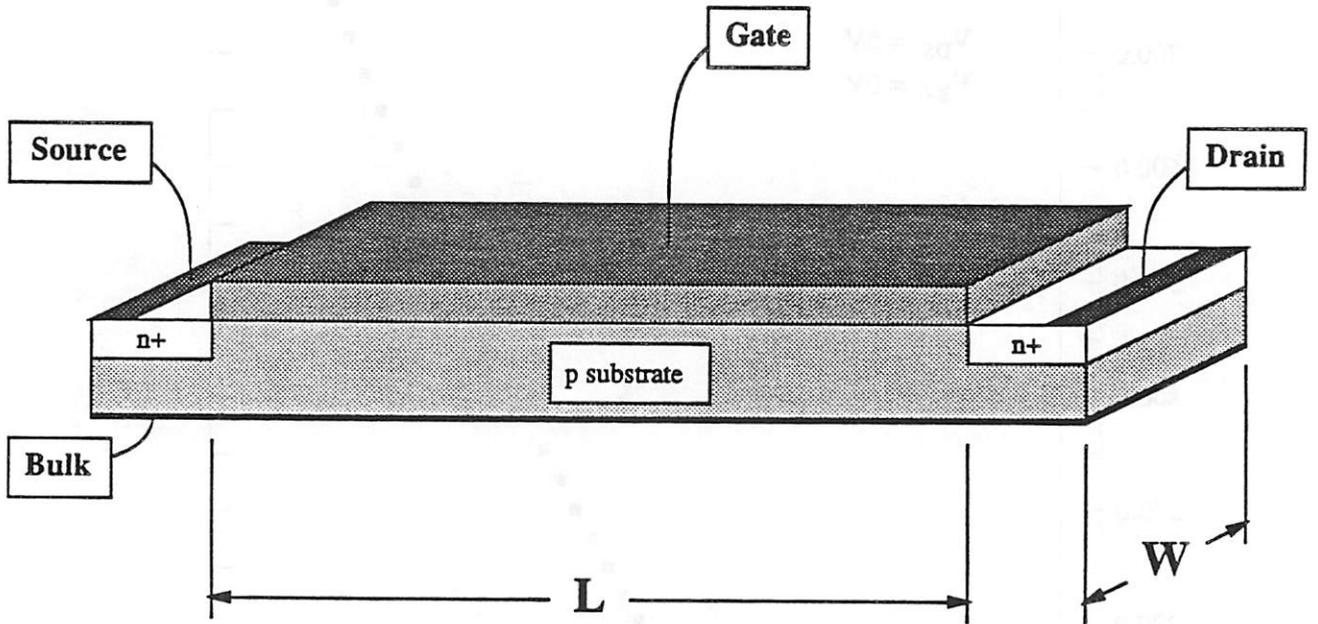
Fig. 5.2: Inversion Layer Grid Structure
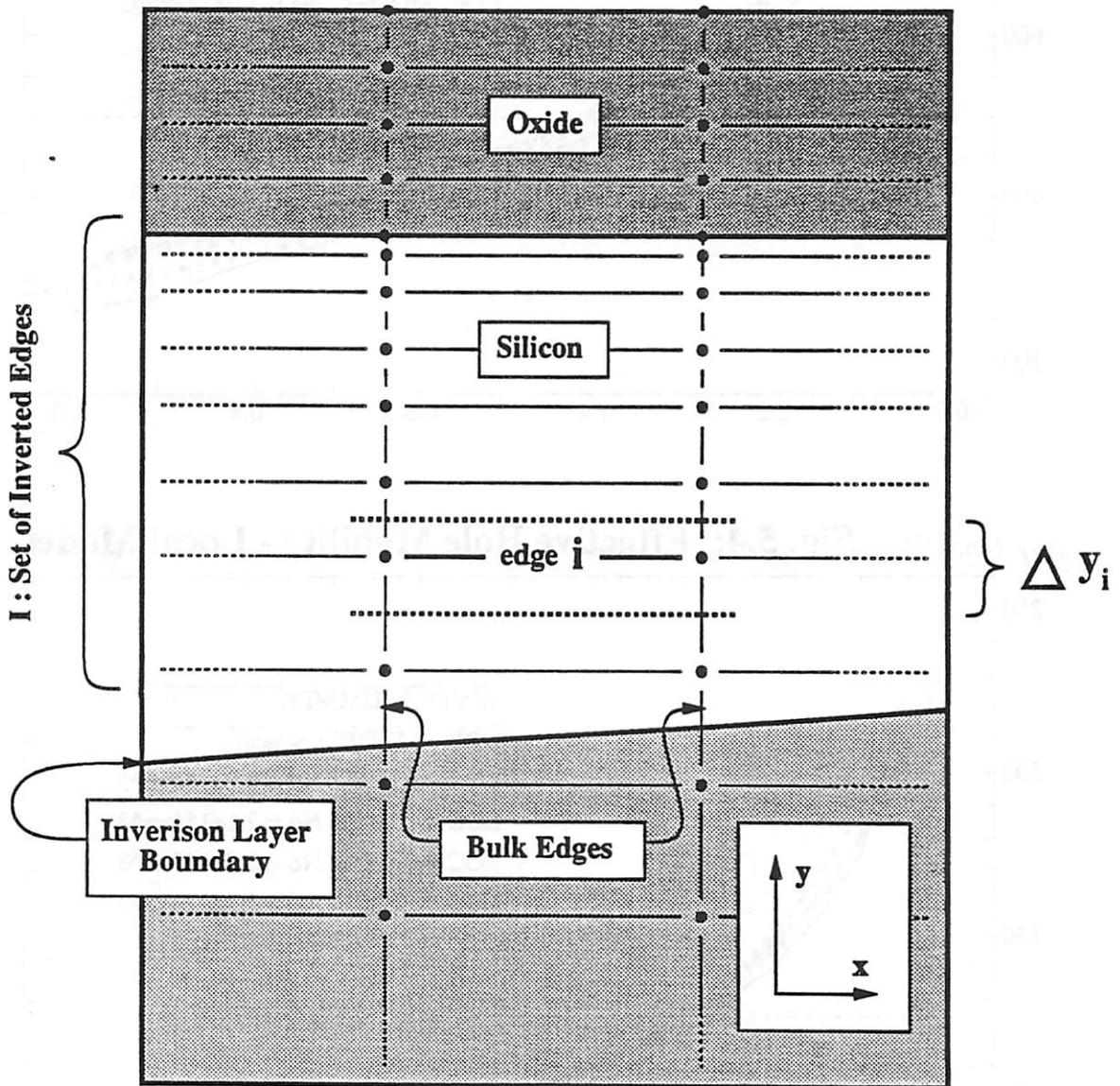
μ_{eff}^n (cm²/Vs) **Fig. 5.3: Effective Electron Mobility - Local Model**

WATT-PLUMMER
ORIG. MODEL: typical
□LOC. MODEL: Na = 3.0e14/cm^3
•LOC. MODEL: Na = 2.2e15/cm^3
×LOC. MODEL: Na = 2.3e16/cm^3
•LOC. MODEL: Na = 2.0e17/cm^3

$E_\perp^{eff}$ (MV/cm)
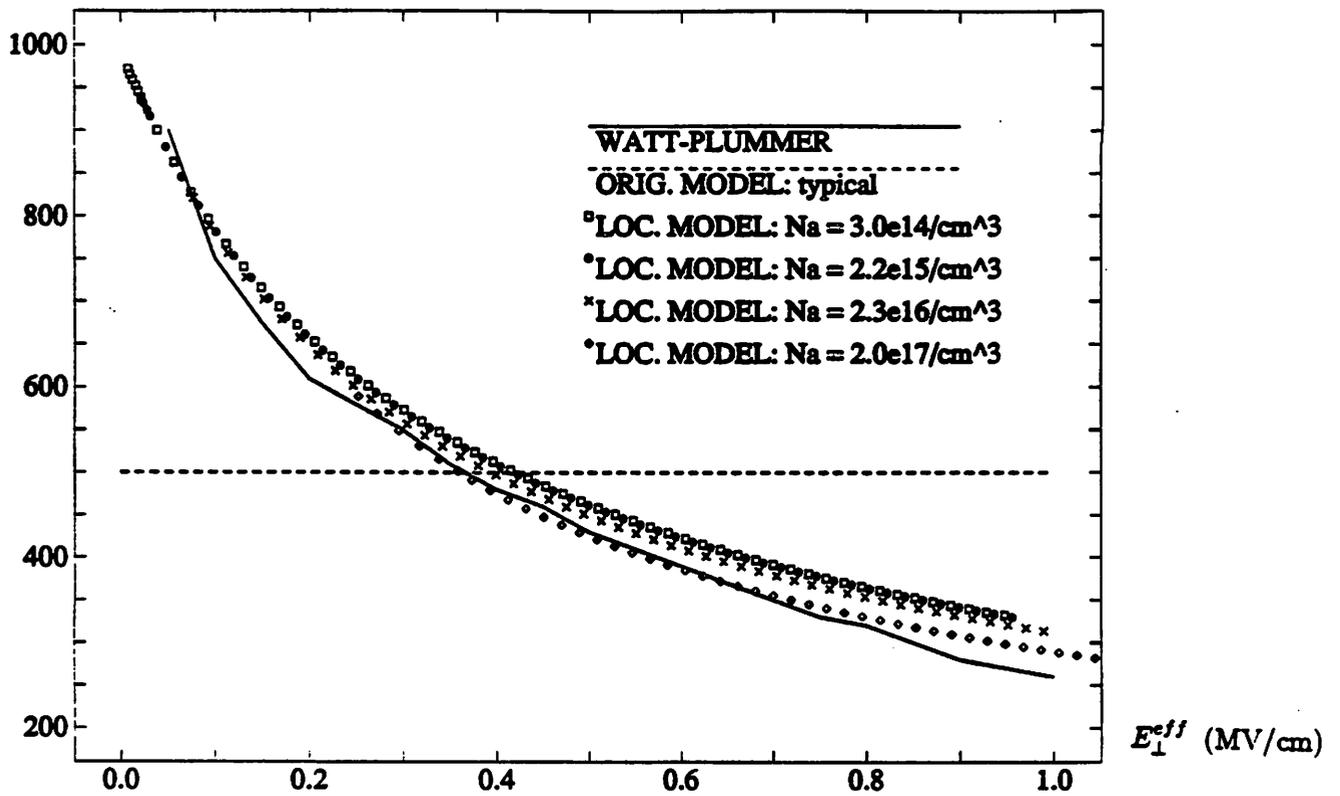
μ_{eff}^p (cm²/Vs) **Fig. 5.4: Effective Hole Mobility - Local Model**

WATT-PLUMMER
ORIG. MODEL: typical
□LOC. MODEL: Nd = 3.0e14/cm^3
•LOC. MODEL: Nd = 2.1e15/cm^3
×LOC. MODEL: Nd = 2.2e16/cm^3
•LOC. MODEL: Nd = 2.1e17/cm^3

$E_\perp^{eff}$ (MV/cm)
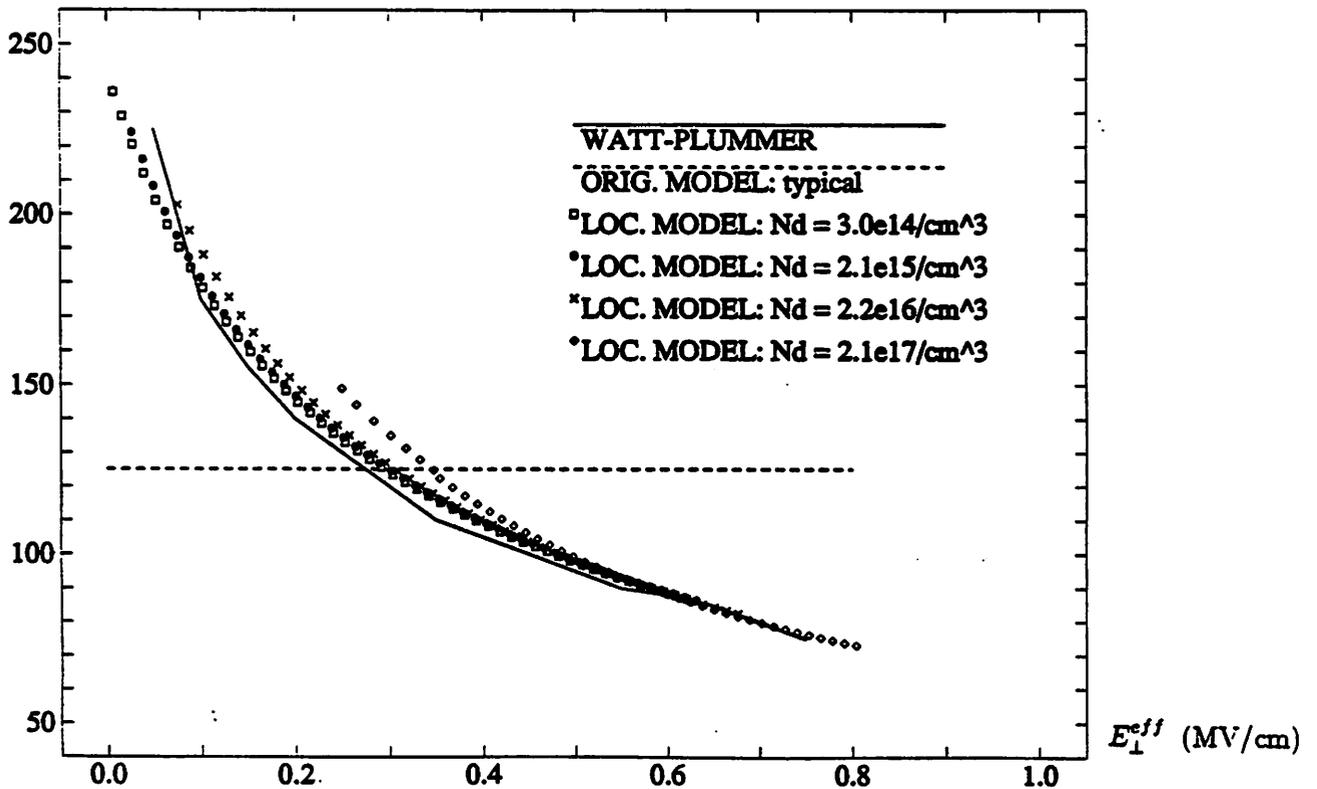
μ^n_{eff} (cm²/Vs) **Fig. 5.5: Effective Electron Mobility - Hybrid Model**

WATT-PLUMMER
ORIG. MODEL: typical
□HYB. MODEL: Na = 3.0e14/cm^3
•HYB. MODEL: Na = 2.2e15/cm^3
×HYB. MODEL: Na = 2.3e16/cm^3
◦HYB. MODEL: Na = 2.0e17/cm^3

$E^{eff}_{\perp}$ (MV/cm)
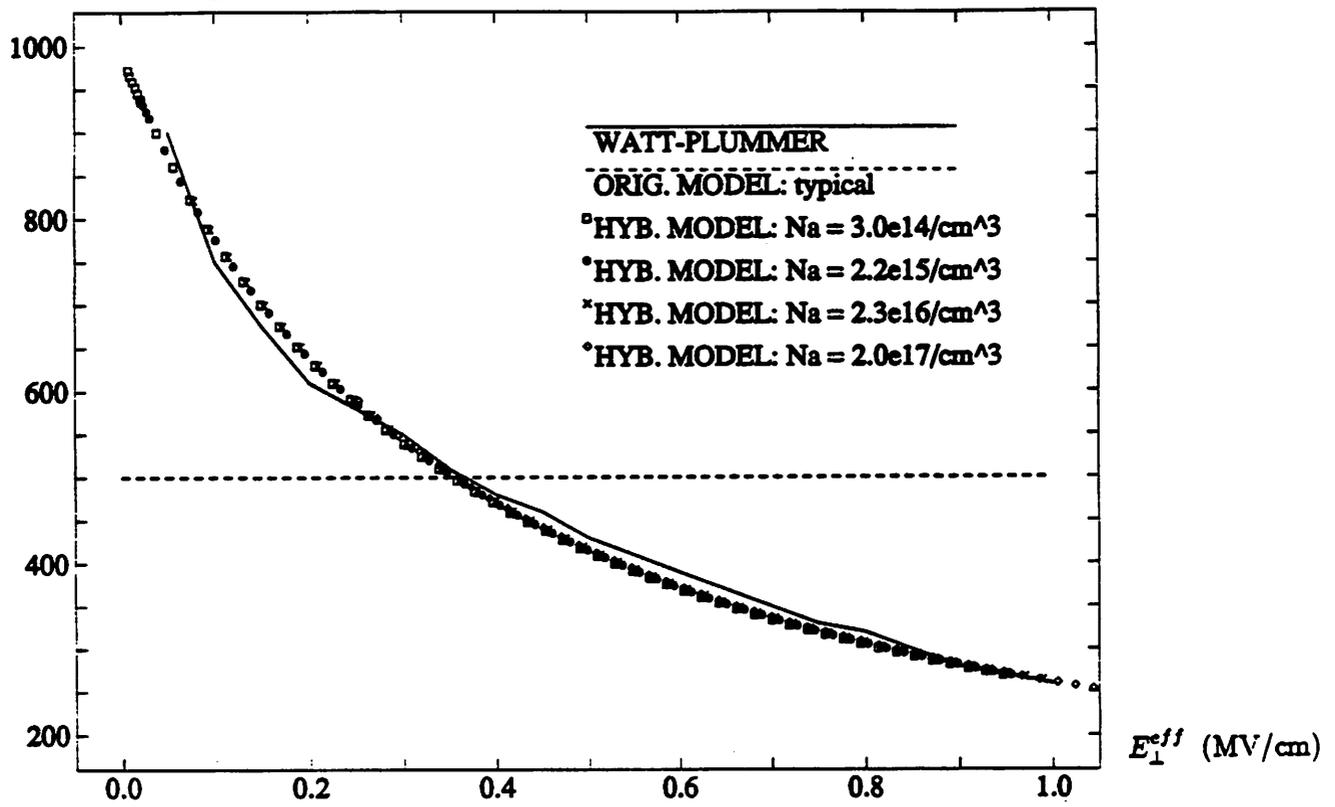
μ^p_{eff} (cm²/Vs) **Fig. 5.6: Effective Hole Mobility - Hybrid Model**

WATT-PLUMMER
ORIG. MODEL: typical
□HYB. MODEL: Nd = 3.0e14/cm^3
•HYB. MODEL: Nd = 2.1e15/cm^3
×HYB. MODEL: Nd = 2.2e16/cm^3
◦HYB. MODEL: Nd = 2.1e17/cm^3

$E^{eff}_{\perp}$ (MV/cm)
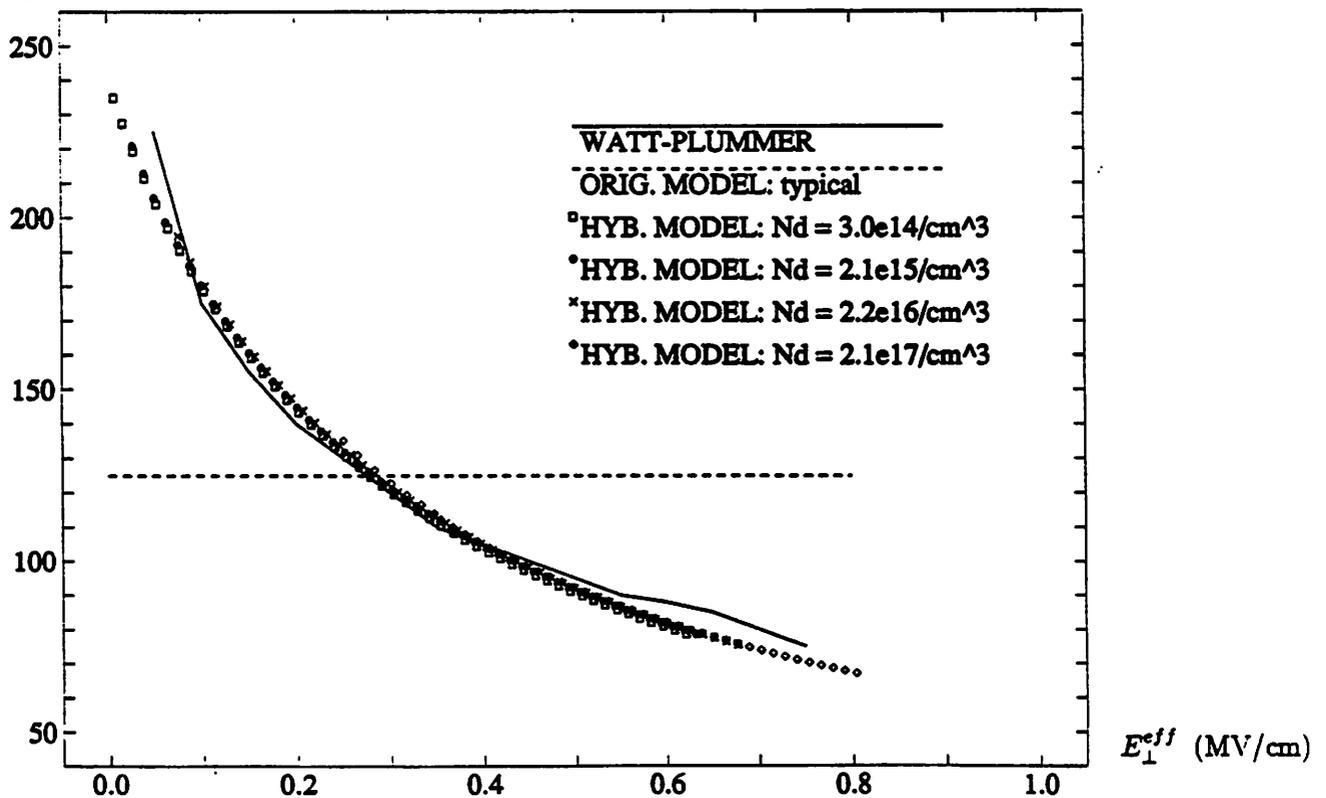
Fig. B.1: Geometry of Example MOSFET

3.0 μm

0.7μm

0.4 μm

0.6 μm

875 Å

n+ : 1e19

n+ : 1e19

0.2 μm

1.1 μm

2.0 μm

p substrate : 2.5e16
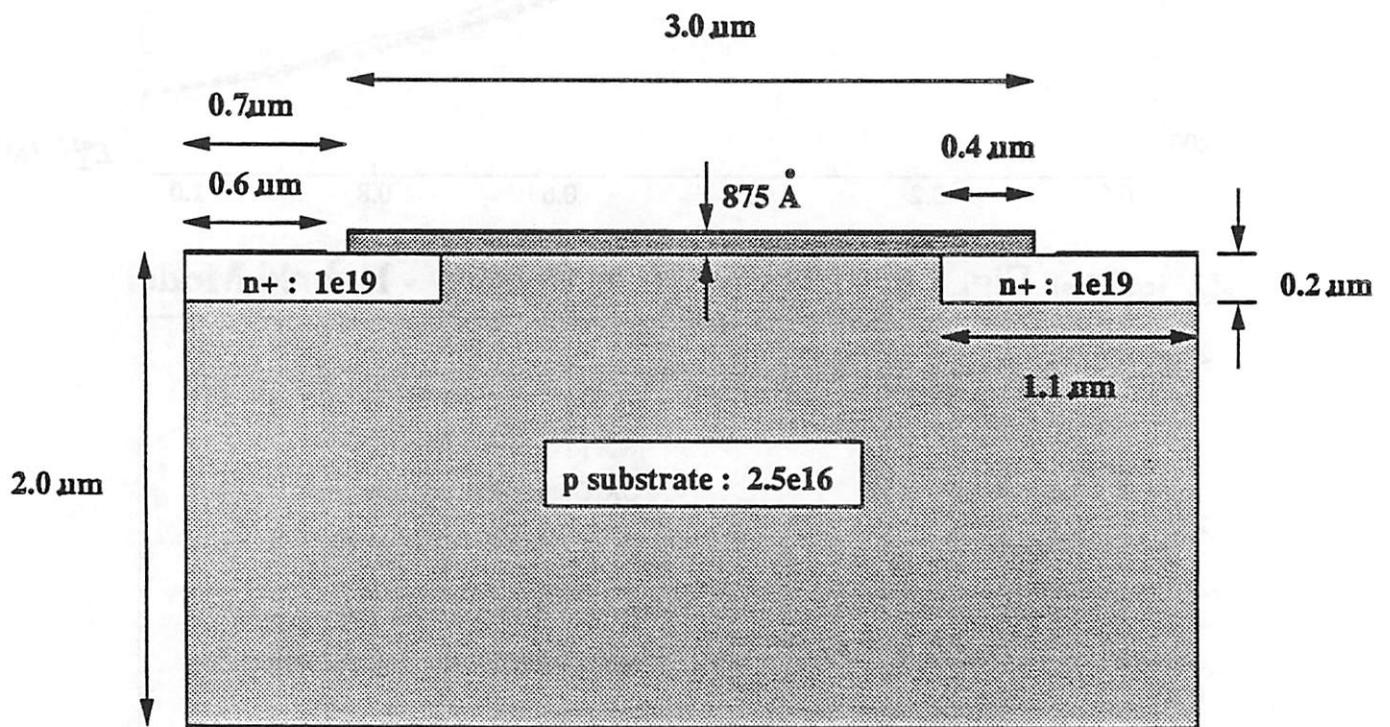
Fig. C.1: MOSFET Simulation Grid
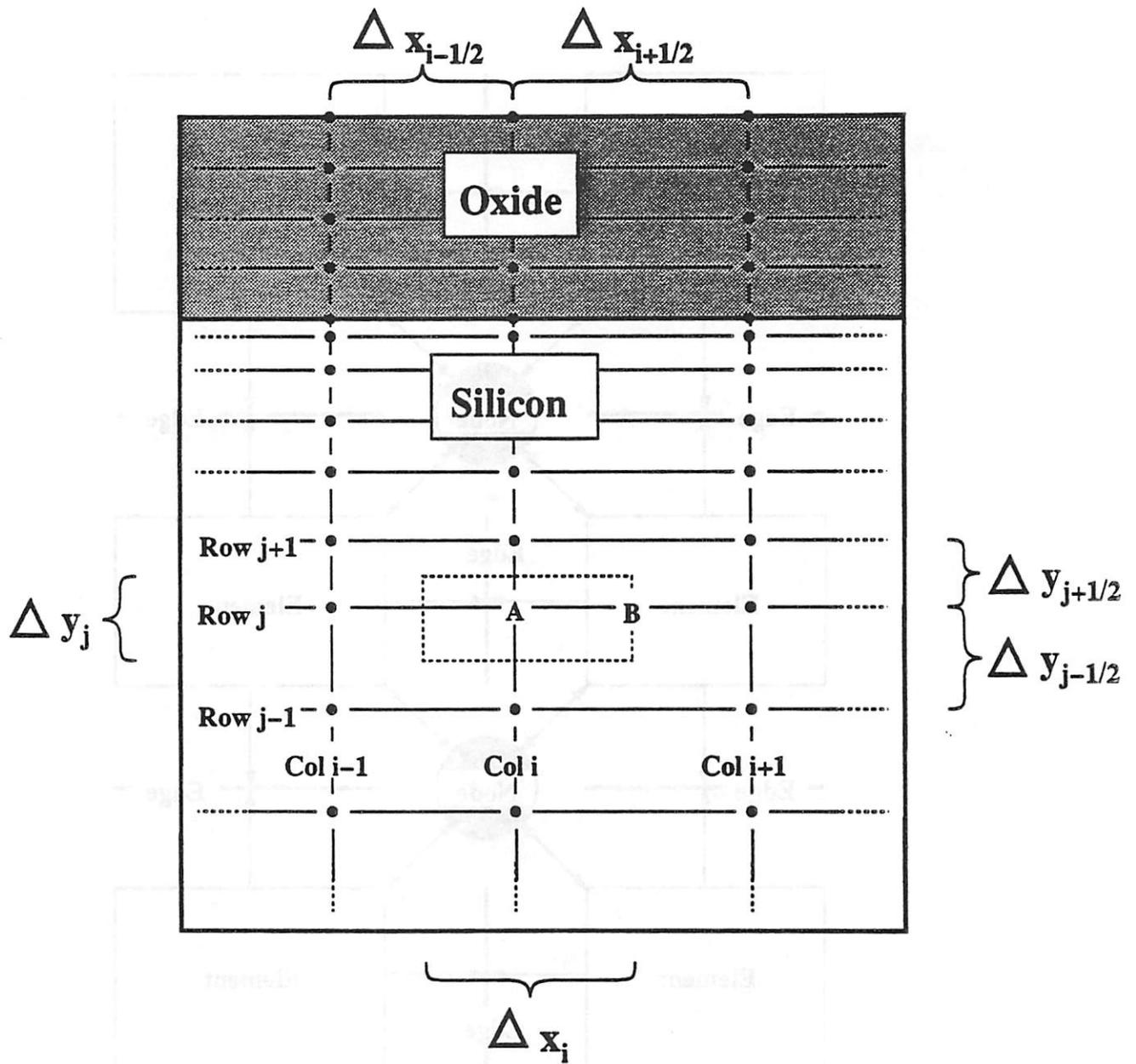
Fig. C.2: DSIM Mesh Data Structures
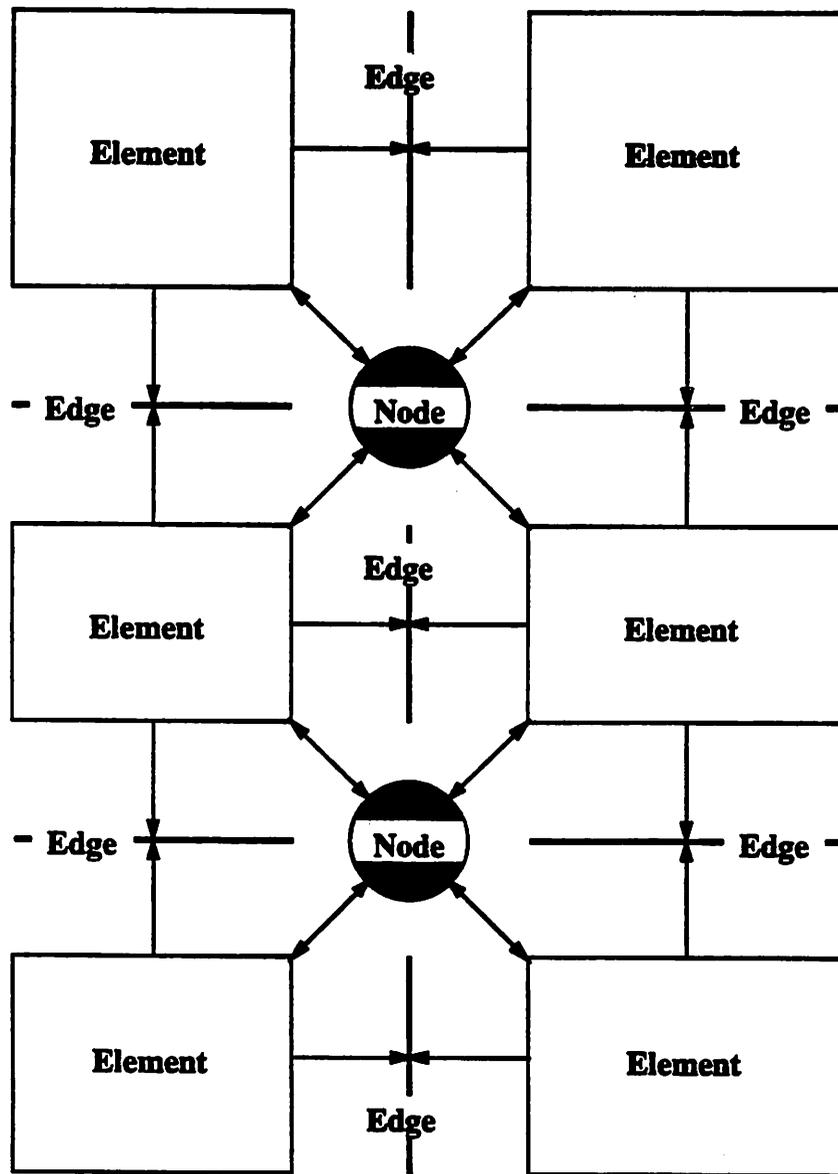
: Arrows indicate Link Pointers between Data Structures